# Remote sensing and inverse transport modeling of the Kasatochi eruption sulfur dioxide cloud

N. I. Kristiansen[1], A. Stohl[1], A. J. Prata[1], A. Richter[2], S. Eckhardt[1], P.Seibert[3], A. Hoffmann[4], C. Ritter[4], L. Bitar[5], T. Duck[5], K.Stebel[1]

[1] Norwegian Institute for Air Research (NILU), Kjeller, Norway.

[2] Institute of Environmental Physics, University of Bremen, Germany.

[3] Institute of Meteorology, University of Natural Resources and Applied Life Sciences (BOKU), Vienna, Austria.

[4] Alfred Wegener Institute, Potsdam, Germany.

[5] Department of Physics and Atmospheric Science, Dalhousie University, Halifax, Nova Scotia, Canada.

**Abstract.**

An analytical inversion method is used to estimate the vertical profile of $SO_2$ emissions from the major eruption of Kasatochi volcano in Alaska in August 2008. The method uses satellite-observed total $SO_2$ columns from GOME- 2, OMI and AIRS during the first two days after the eruption, and an atmospheric transport model, FLEXPART, to calculate the vertical emission profile. The inversion yields an emission profile with two large emission maxima near 7 km above sea level (a.s.l) and around 12 km a.s.l, with smaller emissions up to 20 km. The total mass of $SO_2$ injected into the atmosphere by the eruption was estimated to 1.7 Tg, with ~1 Tg reaching the stratosphere (>10 km). The estimated vertical emission profile was robust against changes of the assumed eruption time, meteorological input data and satellite data used. Using the vertical emission profile, a simulation of the transport extending for one month after the eruption is performed. The simulated plume agrees very well with $SO_2$ columns observed by GOME-2, OMI and AIRS until 6 days after the eruption, and the altitudes agree with both CALIPSO measurements and ground-based lidar observations to within 1 km. The method is computationally very fast. It is therefore suitable for implementation within an operational environment, such as the Volcanic Ash Advisory Centers (VAACs), to predict the threat posed by volcanic emissions for air traffic.

## 1. Introduction

Volcanic eruptions can inject particles and gases high into the atmosphere. Generally, the major component is tephra, also called volcanic ash, which is solidified material. The most abundant gases emitted are water vapour ($H_2O$) and carbon dioxide ($CO_2$). Another important gas emitted by volcanic eruptions is sulfur dioxide ($SO_2$) which is of special concern for the global climate and the ozone layer if it reaches the stratosphere. Explosive volcanic eruptions can emit $SO_2$ to very high altitudes (> 10 km) in contrast to anthropogenic and other emissions which occur mostly at low altitudes.

Airborne volcanic ash is a danger to aircraft because it can cause serious damage, and even loss of power on the engines. There are nine Volcanic Ash Advisory Centers (VAACs) around the world that advise international aviation of the location and movement of volcanic ash clouds. The VAACs use satellite information, ground reports from volcanological agencies, pilot reports, meteorological knowledge and numerical models to track and forecast ash movement so that aircraft can fly around or over the airborne ash safely [*VAAC,* 2008]. A fundamental piece of information required by the VAACs is the height of the ash clouds, as this is the principal determinant of the ash transport and potential hazard to jet aircraft.

For non-explosive volcanic eruptions, the injection height of the emissions is of the order of a few hundred meters and is dominated by thermal plume rise. On the other hand, explosive eruptions have a considerable initial exit velocity, and the high thermal energy in the eruption plumes allows them to quickly reach high altitudes (> 10 km). Generally the injection height depends on the kind of eruption and meteorological conditions (e.g., the horizontal winds,

humidity and thermal stratification) [*Oberhuber et al.*, 1998]. For explosive eruptions characterized by a Volcanic Explosivity Index (VEI) of 2–3 (moderate scale) 20% of volcanic plumes rise higher than 15 km, 60% rise above 10 km, and 80% rise above 6 km [*Halmer and Schmincke*, 2003]. For the eruption of Mount Pinatubo in June 1991 (VEI~6, "colossal"), gas and particles were carried to an altitude of more than 30 km [*McCormick et al.*, 1995]. Once the species are injected into the stratosphere they are rapidly advected around the globe.

Dispersion models can forecast the long-range transport of the emissions. However, one problem is the vertical transport in the eruption column which they cannot explicitly simulate. Thus, the vertical emission profile is needed as an input parameter, which must be determined by other means. Determining the emission height profile of a volcanic eruption is a challenge. In principle, it can be obtained by special models like the Active Tracer High Resolution Model (ATHAM) which can simulate the vertical transport of ash in the eruption column. However, they require accurate estimates of the mass flux of pyroclastic material and other information that is normally not available, especially not on a near-real time basis [*Textor et al.*, 2003; *Oberhuber et al.*, 1998].

Measurements using aircraft [*Mankin et al.*, 1992] and weather radar and lidar observations [*Wang et al.*, 2008] can provide information on the plume height. However, not all locations are covered by such observations. Remote sensing observations from satellites can provide global coverage, but normally they only deliver total columns or very poorly resolved vertical profiles. Also, many instruments operate from low-earth orbits providing only one or two overpasses per day limiting the temporal resolution of the measurements. Other methods can potentially provide

77 information on the $SO_2$ vertical distribution in the lower troposphere by calculating a residual
78 based on $SO_2$ columns from infrared and ultraviolet satellite retrievals [*Carn et al.*, 2008].
79
80 A common technique to estimate the vertical emission profile for the purpose of volcanic plume
81 forecasting involves trial-and-error fits between satellite observations of the total column of
82 volcanic debris and model results based on different assumptions of the emission height. The
83 HYbrid Single-Particle Lagrangian Integrated Trajectory (HYSPLIT) model, for example, can be
84 used with satellite measurements of $SO_2$ from the Ozone Monitoring Instrument (OMI), to fit
85 trajectories at certain altitudes with the observations [e.g., *Carn et al.,* 2008]. The disadvantage
86 with this method is that the model runs and satellite data are matched "by eye". This is a
87 subjective process that is time-consuming and can lead to errors.
88
89 In this paper, we present the vertical emission height profile of $SO_2$ derived through an analytical
90 inversion method. The $SO_2$ is often more easily observed by satellite sensors than ash. While in a
91 sheared atmosphere the ash and $SO_2$ in eruption clouds may travel in different horizontal
92 directions, it is likely that the $SO_2$ is accompanied by some ash. Thus, often $SO_2$ can serve as a
93 proxy for volcanic ash. The $SO_2$ is also important for geochemical and climate modeling in itself.
94
95 The inverse method has recently been developed by *Eckhardt et al.* [2008] and tested in a case
96 study of the 30 September 2007 low-latitude eruption of the Jebel at Tair volcano (15.55°N,
97 41.83°E) located in the Red Sea. The Jebel at Tair eruption was an ideal test case because it
98 provided excellent observation conditions for satellite remote sensing (a dry cloudless
99 atmosphere) and very good coverage by such observations. For this paper, which is based on the

first author's master thesis [*Kristiansen,* 2009], the inverse method is tested for the high-latitude eruption of Kasatochi Volcano in August 2008. The observation conditions for this eruption were more difficult and, thus, provide a more demanding test case for the inverse method.

## 2 Kasatochi Volcano, Alaska

Kasatochi Volcano (52.17°N, 175.51°W) is a small (2.7×3.3 km) unpopulated island volcano situated on the Aleutian arc. The active stratovolcano reaches only 314 m above sea level (a.s.l) [*Smithsonian Institution*, 2008]. From 7-8 August 2008 Kasatochi volcano erupted with little warning after lying dormant for more than 200 years [*Alaska Volcano Observatory*, 2008]. The eruption emitted 1.2 – 2.5 Tg of $SO_2$ to the atmosphere [e.g., *Prata et al.*, 2009; *NASA,* 2008; *Karagulian et al.,* 2009; *Richter et al,* 2009a; *Rix et al.,* 2008], which is the largest $SO_2$ mass loadings since Chile's Hudson volcano erupted in 1991. The eruption also injected an amount of ash into the atmosphere [*Prata et al.*, 2009] and Alaska Airlines was forced to cancel 44 flights between 10 and 11 August 2008 [*O'Malley and Bragg*, 2008]. The ash particles were deposited after a few days, while the $SO_2$ dispersed throughout the northern hemisphere. *Theys et al.* [2009] also reported large enhancements of bromine monoxide (BrO) seen in satellite data in the vicinity of Kasatochi in the days following the eruption.

The Alaska Volcano Observatory (AVO) reported that three distinct explosive eruptions occurred at Kasatochi at approximately 22:01 UTC on 7 August, 01:50 UTC and 04:35 UTC on 8 August [*Waythomas et al.*, 2008]. The first two events produced relatively ash-poor, but gas-rich eruption clouds that reached approximately 14.5 - 16.5 km a.s.l. The third event generated an ash- and gas-rich plume that rose to about the same altitude, and was followed by about 17

hours of continuous ash emission as determined from satellite data. *Prata et al.* [2009] show that the ash and $SO_2$ erupted from Kasatochi was collocated and could be observed to travel together for at least 3 days following the 8 August eruptions, thus $SO_2$ may serve as an appropriate proxy for ash in this case.

Synoptic maps of geopotential heights of the pressure levels 1000 hPa and 500 hPa shortly after the first eruption, taken from the European Centre for Medium-Range Weather Forecasts (ECMWF) analysis, are shown in Figure 1. A low pressure system was passing over the area in the hours of the eruptions, which generated a distinct circular shaped $SO_2$ plume, as seen from the AIRS satellite measurements. The thermal tropopause height around the Kasatochi volcano, given by the ECMWF data, was about 10 km. Given the reported injection height from AVO (~14.5 - 16.5 km) the debris from the eruption penetrated into the stratosphere.

## 3. Atmospheric transport modeling

In this study the Lagrangian particle dispersion model FLEXPART ([*Stohl et al.,* 1998, 2005], see also http://transport.nilu.no/flexpart) was used to simulate the transport of $SO_2$ emitted by the eruption of Kasatochi volcano. The model was first described and validated by *Stohl et al.* [1998] with data from continental-scale tracer experiments and is now used for a large range of applications, including simulating the dispersion of volcanic plumes [*Prata et al.*, 2007; *Eckhardt et al.*, 2008].

FLEXPART calculates trajectories of "tracer particles" (not necessarily representing real particles, but infinitesimally small air parcels) as they are displaced by the winds.

For this study, the model simulations were based on meteorological analysis data provided by ECMWF [*ECMWF*, 2002]. The global ECMWF data has 91 vertical levels, and 1°×1° horizontal resolution. A nest with higher resolution of 0.5°×0.5° was used for the area of interest (the eastern North Pacific region: 180°W-120°W, 40°N-60°N). Analyses at 00:00, 06:00, 12:00 and 18:00 UTC as well as 3-h forecasts at intermediate times were used. We also made alternative FLEXPART simulations using input data from the National Centers for Environmental Prediction Global Forecast System (GFS) model with 0.5°×0.5° resolution at 26 pressure levels.

Trajectories of $SO_2$ tracer particles are calculated using the mean winds interpolated from the analysis fields as well as random motion representing turbulence [*Stohl and Thompson*, 1999]. For moist convective transport, FLEXPART uses the scheme of *Emanuel and Živković-Rothman* [1999], as implemented and tested in FLEXPART by *Forster et al.* [2007].

In the atmosphere, $SO_2$ is lost by reaction with OH, dry deposition, and aqueous-phase chemical reactions. Monthly averaged three-dimensional OH concentration fields provided from the GEOS-CHEM model [*Bey et al.*, 2001], were used to determine tracer mass loss by reaction with OH. This process is most important in the troposphere. Aqueous-phase chemical reactions were not considered in the model simulations. Dry deposition of $SO_2$ was calculated with the resistance method [*Wesely and Hicks*, 1977] using data from *Wesely* [1989] with updates.

FLEXPART model runs were used as input to the inversion method to explore the sensitivity of downwind $SO_2$ total columns to the altitude and mass of the initial emissions. Fifty releases were configured in vertically stacked emission layers of 500 m thickness between the model ground

and 25 km above the volcano. In each of these layers, 300 000 tracer particles were released uniformly along a vertical line source and subsequently tracked in the model atmosphere. Three different simulations were executed with particles released at the times of the eruption onsets as reported by AVO; on 7 August 22:01 UTC, 8 August 01:50 UTC and 04:35 UTC. The simulation extended for 2 d after the eruption onset. Concentrations were calculated as hourly means throughout the simulation. The output grid was 0.5° ×0.5° horizontally, with 9 vertical layers of 2 km resolution between 4 km and 22 km, a single layer between the surface and 4 km, and another layer from 22-50 km a.g.l. From this model output, total atmospheric columns were computed using averaging kernels as described in Section 4.4. The simulations can be viewed as source-receptor relationships which measure the sensitivity of a column value to the emission strength in each of the emission layers. Using these sensitivities and satellite observations of total $SO_2$ columns, the inversion finally yields estimates of the actual mass injected in each of the layers above the volcano.

After applying the inversion method and obtaining the estimated emission profile of $SO_2$, a longer FLEXPART simulation of the transport was performed. This simulation extended over one month following the eruption onset and was used for validation of the estimated profile by comparison with independent observations.

## 4. Remote Sensing Data

Several satellite instruments made measurements of the $SO_2$ released by the eruption of Kasatochi Volcano over the days following the eruption. For this study we have utilized both ultraviolet and infrared satellite retrievals of $SO_2$. The instruments measuring in the ultraviolet

192 spectral region include the Global Ozone Monitoring Experiment-2 (GOME-2) and the Ozone
193 Monitoring Instrument (OMI), while the Atmospheric Infra-Red Sounder (AIRS) provides
194 infrared measurements.
195
196 All of the instruments deliver total or partial column measurements with little vertical resolution.
197 The infrared retrievals provide partial column measurements due to very low sensitivity to $SO_2$
198 in the moist lower troposphere, while the ultraviolet retrievals can detect $SO_2$ down to the
199 ground. Depending on which altitude the $SO_2$ is located and on other factors such as the
200 temperature and humidity profiles, the different retrievals may yield different column amounts.
201 One big advantage of the AIRS retrievals is the ability to make observations also during
202 nighttime, while the ultraviolet measuring instruments are restricted to daytime observations with
203 high solar elevation. All satellite data were re-sampled to the FLEXPART 0.5° ×0.5° output grid.
204
205 In addition, the Infrared Atmospheric Sounder Interferometer (IASI) provided measurements of
206 the eruption of Kasatochi which were utilized by *Karagulian et al.* [2009] to retrieve a coarse-
207 resolution vertical profile of $SO_2$. This profile has been applied to our inversion algorithm as *a*
208 *priori* information.
209
210 **4.1. GOME-2**
211 The GOME-2 instrument is a UV/visible spectrometer covering the wavelength region of 240 -
212 790 nm at a moderate spectral resolution of 0.2 - 0.4 nm with a ground-pixel size of 80 x 40 $km^2$
213 over most of the globe [*Munro et al.*, 2006]. With its large swath, GOME-2 provides global
214 coverage nearly daily. $SO_2$ retrievals are performed with a variant of the Differential Optical

Absorption Spectroscopy (DOAS) method. Using the spectral window of 312.5 - 327 nm, tabulated slant optical depths of $SO_2$ and ozone are fitted to the observed optical thickness. For the initial iteration, an *a priori* of 1 Dobson Unit (1DU=$2.69\times10^{16}$ molecules/$cm^2$) $SO_2$ vertical column is used. Depending on the retrieved column, a new $SO_2$ optical depth is selected based on a more appropriate *a priori*. This procedure is repeated until closure is found between the retrieved and the *a priori* column. This iterative retrieval approach is necessary as $SO_2$ becomes a strong absorber in the UV at the high column amounts experienced during the Kasatochi eruption and ignoring this effect leads to strong underestimation of the total column. Similar approaches have been proposed by *Richter et al.* [2006] and *Yang et al.* [2007] for situations with much less $SO_2$. After the main retrieval, each orbit is post processed to remove a small latitudinal offset in the $SO_2$ columns by applying a median filter over ±10°latitude. This correction is similar to the one applied to OMI $SO_2$ data [*Yang et al.*, 2007] and is negligible compared to the columns discussed here. Details on the retrieval can be found in *Richter* [2009b]. As discussed in *Yang et al.* [2007], both the vertical distribution of $SO_2$ and the ozone column also impact on the results. Here, the US standard atmosphere has been assumed for $O_3$ and an $SO_2$ plume of 1 km thickness centered at an altitude of 10.5 km. These constant assumptions together with the impact of clouds and aerosols which have not been accounted for lead to a relatively large uncertainty of the $SO_2$ columns retrieved in the Kasatochi plume. We estimate this uncertainty to be of the order of 10% in the plume while the noise level outside the plume is better than 1 DU for individual measurements. Maximum $SO_2$ mass loadings for the eruption of Kasatochi were found to be up to about 2.5 Tg from GOME-2 [*Richter et al.*, 2009a].

237 **4.2. OMI**

238 The OMI instrument on board the EOS/Aura satellite was designed principally for measuring
239 global ozone, but with secondary goals of measuring other trace gases, including $SO_2$. It
240 measures solar back-scattered radiation in the UV between 270 and 365 nm. The daytime
241 equator crossing time is 10:45 UTC, the nadir pixel size is $13 \times 24$ km$^2$ and the swath width is
242 2600 km which provides once-daily global coverage.

243

244 $SO_2$ column data from OMI are produced using the Band Residual Difference (BRD) algorithm
245 [*Krotkov et al.*, 2006] and the Linear Fit (LF) algorithm [*Yang et al.*, 2007]. For this study we
246 used the product estimate of the column density of $SO_2$ for the upper tropospheric and
247 stratospheric $SO_2$ (ColumnAmountSO2_STL). The retrieval used for determining $SO_2$ from OMI
248 exploits the $SO_2$ absorption features between 310 and 340 nm. The effect of absorption by ozone
249 in the same spectral region, and also effects of Rayleigh multiple scattering, the "Ring effect"
250 and the geometrical air-mass factor have been accounted for in the algorithm. For large $SO_2$
251 columns (>100 DU), such as for Kasatochi, the retrieval error increases and the algorithm
252 underestimates the true $SO_2$ amount. An overall uncertainty of 14 % for the OMI retrievals is
253 assumed to be appropriate for the large $SO_2$ columns for Kasatochi [*K.Yang* (pers.comm) and
254 *Yang et al.*, 2007]. Maximum $SO_2$ mass loadings for the eruption of Kasatochi were found to be
255 about 1.4 Tg from OMI (*NASA* [2008] and
256 http://earthobservatory.nasa.gov/IOTD/view.php?id=8998).

257

258 **4.3. AIRS**

259 The AIRS instrument on board the EOS-Aqua polar orbiting satellite was able to clearly detect
260 the $SO_2$ cloud from Kasatochi for about 1 week and less well in the following weeks as the cloud
261 diluted and moved over Europe and on to Russia. The IR retrievals have less sensitivity than the
262 UV retrievals and thus AIRS cannot detect the $SO_2$ for as long as OMI or GOME-2. The AIRS
263 instrument has high spectral resolution and is operating at infrared wavelengths between 3.7 and
264 15.4 $\mu m$ [*Chahine et al.*, 2006]. The swath width is ±49° from nadir producing nadir pixels with
265 dimensions $15 \times 15$ km$^2$, increasing to $18 \times 40$ km$^2$ at the swath edge. The $SO_2$ partial column
266 abundances were determined by use of the retrieval scheme developed by *Prata and Bernardo*
267 [2007]. The algorithms for determining $SO_2$ from AIRS exploit the strong $SO_2$ anti-symmetric
268 absorption feature near 7.3 $\mu m$, but because water vapour also absorbs strongly across this band,
269 the retrievals are restricted to regions of the atmosphere that are relatively dry, i.e. - the upper
270 troposphere (heights > 3 km) and lower stratosphere. AIRS error estimates for an individual
271 pixel are at worst ±6 DU, and typically ±3 DU [*Prata and Bernardo*, 2007].
272
273 Maximum UTLS mass loadings were found to be ~1.2 Tg from this instrument, which is lower
274 than that found using ultra-violet measurements. The difference is mostly due to the lower
275 sensitivity to pixels with low $SO_2$ amounts (<3 DU), the narrow AIRS swath width, which
276 sometimes excluded portions of the plume and to a lesser extent the penetration depth of the
277 AIRS measurements. For $SO_2$ clouds that are high and thick, it is possible for the IR bands to
278 saturate and an upper limit on $SO_2$ detection is reached. Examination of the AIRS IR spectra
279 suggests that this did not occur in the case of Kasatochi.

280 Table 1 gives an overview of the estimates of total mass emitted from the eruption of Kasatochi,
281 derived from various satellite retrievals.
282
283 **4.4. Height sensitivity**
284 The satellite retrievals depend on a number of factors such as the wavelength region of the
285 satellite measurements, the atmospheric temperature profile and the vertical distribution of all
286 absorbing gases. This implies that the magnitude of the observed $SO_2$ signal does not only
287 depend on the total $SO_2$ amount in the atmosphere but also on its vertical distribution which
288 cannot be obtained from the measurements themselves. Thus, in the satellite retrievals of $SO_2$
289 certain assumptions have to be made about the height of the $SO_2$ cloud. In regard to this, the
290 weighting function and averaging kernel are used as described by *Rodgers* [2000] (page 15, 56,
291 and 223). The weighting function represents the radiance contribution from a layer at a certain
292 height level to the total radiance sensed by the satellite. The averaging kernel is the sensitivity of
293 the retrieval to the true state and is needed in comparisons between in situ profile measurements
294 and satellite retrievals and in application of data assimilation.
295
296 We use the averaging kernels shown in Fig. 2 when comparing satellite data and model data.
297 Because the vertical sensitivities of the various satellite retrievals are variable, it would be
298 inaccurate to directly compare the reported total columns with total columns obtained from
299 FLEXPART. Instead, it is necessary to sample the FLEXPART $SO_2$ concentration vertical
300 profile with the corresponding averaging kernel of the satellite retrieval.
301

For the AIRS satellite data, we use an averaging kernel for a band-averaged channel at around 7.3 $\mu m$ for a perturbed atmosphere with a layer of $SO_2$ present at 15 km. In practice the 7.3 $\mu m$ channel is sensitive to the absorption of both water vapour and $SO_2$, which means that whenever $SO_2$ and water vapour are collocated it is difficult to quantify the $SO_2$. However, the two-step retrieval procedure devised by *Prata and Bernardo* [2007] accounts for both $SO_2$ and water vapour simultaneously.

For UV retrievals, the averaging kernel depends also on surface albedo and $O_3$ column, but it is in particular the atmospheric $SO_2$ profile that is problematic in the presence of large $SO_2$ amounts as the atmosphere below a thick $SO_2$ layer is basically shielded from the satellite view. For GOME-2, we approximate the averaging kernel by a single calculation performed at 317 nm for a UV surface albedo of 0.03 and a 1 km thick $SO_2$ column of 200 DU. For OMI, the height sensitivity is explained by *Yang et al.* [2007]. For this study we have used an averaging kernel for a cloud-free pixel with a surface reflectivity of 0.1 and a prescribed $SO_2$ profile in Umkehr layer 3 (see Fig. 7 of *Yang et al.* [2007]).

Ideally, one should use a different averaging kernel for each pixel to account for regional variability. However, in this study, only one typical averaging kernel for each of the three satellite data sets was employed.

### 4.5. Lidar measurements

The Kasatochi plume was observed with both ground-based and satellite-based aerosol lidar instruments. The Cloud-Aerosol Lidar with Orthogonal Polarization (CALIOP) lidar on board the Cloud-Aerosol Lidar and Infrared Pathfinder Satellite Observation (CALIPSO) satellite made measurements of the Kasatochi eruption clouds several times in the weeks after the eruption. CALIPSO was launched in 2006 and flies as a part of the A-train at 705 km altitude in a 98°-inclination sun-synchronous polar orbit. The equator-crossing time is at 10:30 UTC with a 16-day repeat cycle. CALIOP provides profiles of backscatter at 532 nm and 1064 nm, as well as the degree of the linear polarization of the 532 nm signal. It is a nadir-only looking instrument (60 m pixel size spaced 330 m apart) providing a curtain of measurements with a vertical resolution of 30–300 m. We have utilized the primary level 1 data products of total attenuated backscatter at 532 nm and 1064 nm. The attenuated backscatter profile is the calibrated, range-corrected, laser energy normalized, baseline-subtracted lidar return signal (see *Hostetler et al.* [2006] for more details).

The Dalhousie Raman Lidar at Halifax, Nova Scotia (44.6°N, 63.6°W), Canada, observed the debris from Kasatochi for several months after the eruption. The instrument is described by *Bitar* [2009]. It employs a frequency-doubled Nd:YAG laser transmitting pulses of 532 nm light into the atmosphere at a frequency of 20 Hz, and a 25 cm telescope with photomultipliers and fast counting electronics in the receiver. Profiles of the aerosol extinction coefficient are derived from the measured elastic lidar signals using the Klett inversion technique [*Klett*, 1981]. A constant aerosol extinction-to-backscatter (lidar) ratio of 40 sr was assumed, which is consistent

344 with the lidar ratio observed for stratospheric aerosols after volcanic eruptions [*Jäger and*
345 *Deshler*, 2002, and references therein].
346
347 The AWIPEV station, operated by AWI (Alfred-Wegener-Institute for Polar and Marine
348 Research) and IPEV (Institut polaire français Paul-Emile Victor) in Ny-Ålesund (78.9°N,
349 11.9°E) on Svalbard observed the Kasatochi plume using the Koldewey-Aerosol-Raman-Lidar
350 (KARL). KARL is a backscatter-Raman lidar determining the concentration of aerosols in the
351 atmosphere using a pulsed Nd:YAG laser which emits beside the 1064 nm fundamental laser line
352 the frequency doubled (532 nm) and tripled (355 nm) laser lines with a pulse repetition
353 frequency of 50 Hz. The receiving telescope has a diameter of 30 cm (for further details, see
354 *Hoffmann et al*, [2009]). The aerosol backscatter coefficient is calculated with the Klett
355 algorithm [*Klett,* 1981] based on 10 minute integrated profiles with a vertical resolution of 60 m.
356
357 The lidar measurements were used to validate the height of the simulated $SO_2$ plume. The
358 aerosol extinction coefficient is roughly proportional to the total aerosol mass and was used as a
359 proxy of the sulphate concentrations in the atmosphere. Aerosols are formed by the conversion
360 of $SO_2$ to sulphate and the validation was done by comparing the lidar measurements with the
361 $SO_2$ concentration simulated by FLEXPART. The comparison is qualitative as aerosol extinction
362 coefficient and concentration of $SO_2$ are two different quantities. However, because one is
363 formed from the other, it is expected that $SO_2$ and aerosols are at the same altitude.
364

## 5. Inversion algorithm

The inversion method used in this study is based on work of *Seibert* [2000] and has been expanded and described recently by *Eckhardt et al.* [2008]. They improved it to allow for an *a priori* for the unknown sources, a Bayesian formulation considering uncertainties for the *a priori* sources and the observations and an iterative algorithm for ensuring a solution with only positive values. A major advantage of this algorithm is that it provides an almost entirely analytical solution of the optimization problem, making it very fast and reliable.

Like in other inverse problems [e.g., *Menke*, 1984], we have observations that depend on a number of control variables through a physical process which can be quantitatively simulated. Here, the observations are sets of (weighted) $SO_2$ column values, the control variables are the $SO_2$ emission rates as a function of height (and possibly time) on a discrete raster, and the physical process is the transport, diffusion and transformation of $SO_2$ in the atmosphere.

The optimum solution (values of the control parameters) is defined as that which leads to the best agreement between observed and simulated values. “Best” agreement is measured as the sum of the squared differences. Different to the ordinary Root Mean Square Errors (RMSE), however, we are taking into account uncertainty variances as weights for forming the sum. This leads to a “most likely” solution in the statistical sense, provided at least that the errors are normally distributed and independent.

If there were sufficient observation data and not too many unknown control variables, this would be enough to obtain a solution to our problem. Minimising the cost function consisting of the

388 weighted squared errors yields a linear system of equations that can be solved analytically with
389 standard linear algebra methods and software tools. However, if we construct the vector of
390 unknowns as a simple stack of emissions in equidistant vertical layers, we could easily find that
391 some parts, e.g. close to the ground (low sensitivity of the satellite retrievals) or at high levels
392 near or above the top of the eruption column (small wind shear), are not well constrained by
393 observations. This could render the solution unstable, even if the number of known variables
394 exceeds well the number of unknowns, leaving us with a so-called ill-conditioned inverse
395 problem. To prevent this, some form of *a priori* knowledge has to be added.
396
397 In the method used here, two forms of *a priori* knowledge are used. One is a prescribed estimate
398 of the emission profile (typically very smooth, possibly vertically constant) together with an
399 uncertainty (usually formulated as a fraction of the first-guess estimate). The other is the
400 assumption that the vertical profile is not zig-zagging wildly, mathematically expressed as a
401 small absolute value of the second derivative. Both assumptions provide additional terms to be
402 added to the cost function and can be formulated as linear operators on the vector of unknowns.
403 Thus, we can still proceed with the same standard solution method.
404
405 The mathematical formalism would allow negative values to occur in the solution. To render the
406 solution more physically meaningful, we use an iterative process to reduce the uncertainty of the
407 first-guess where the solution is negative until the resulting solution is not negative.
408
409 All the mathematical details can be found in *Eckhardt et al.* [2008]. What remains is the proper
410 specification of the *a priori* profile and the uncertainties (weights). For this study, the *a priori*

411 emissions were based on the shape of a coarse-resolution IASI $SO_2$ profile estimated by
412 *Karagulian et al.* [2009], which shows a broad maximum centered around 12 km. The total mass
413 of the *a priori* profile was specified to 1.3 Tg, which is in agreement with the minimum of the
414 satellite emission estimates (see Table 1). The *a priori* uncertainties were chosen to allow
415 substantial corrections to the initial profile (see Figures 4 and 6).
416
417 The standard errors of the observations should contain not only the uncertainty of the retrieved
418 $SO_2$ columns but rather be standard misfit between the observations and the model results.
419 Because detailed error statistics are lacking, we assume that a large part of the error stems from
420 the model simulation. For the UV satellite data, with an overall uncertainty of the retrievals of
421 about 10-14 %, we used a standard error of 20% of the individual pixel value plus 3 DU, giving a
422 minimum of 3 DU uncertainty for all pixels. For AIRS, a 30% + 3 DU uncertainty was chosen
423 based on the instrument's poorer sensitivity.
424
425 The algorithm presently does not give an explicit estimate of the uncertainty of the solution.
426 However, we examine its uncertainty by performing multiple inversions with different data sets
427 and model results.
428

## 6. Results and discussion

### 6.1. Comparison of satellite data

$SO_2$ column amounts retrieved from GOME-2, OMI and AIRS approximately 2 days after the eruption, between 20:53 UTC on 9 August and 00:13 UTC on 10 August are shown in Figure 3. The plume has mainly drifted southeastward from the volcano over the Pacific Ocean. The $SO_2$ distributions obtained from the three instruments are qualitatively similar, but the absolute values vary. For instance, the maximum GOME-2 and OMI columns are, respectively, about four times larger and two times larger than the maximum AIRS column.

The reasons for the discrepancies between the different satellite data sets are not entirely clear. However, since AIRS retrievals give only partial $SO_2$ columns, with $SO_2$ in the lower troposphere not being captured, a negative bias of the AIRS columns was expected. Also since the GOME-2 retrieval accounts for nonlinearities in the absorption and light path, this results in higher $SO_2$ values than for OMI. The different pixel sizes, sampling times and different sensitivities to low $SO_2$ amounts also contribute to the differences between instruments.

It is clear that the biases between the different satellite data sets will cause problems when they are used jointly in the inversion procedure. Ideally, one should apply bias corrections before using these data for the inversions. However, it is not clear which data set should best serve as a reference and the factors determining the biases are not completely understood. Furthermore, the biases cannot easily be described with constant scaling factors. Therefore, we have used the satellite data without bias corrections and leave this task for the future.

### 6.2. $SO_2$ emission height profiles

Satellite data for up to two days after the eruption were used for the inversions. During that time interval, seven, two and four overpasses over the Kasatochi $SO_2$ plume were available for AIRS, OMI and GOME-2, respectively. In addition to using three different satellite data sets, inversions were performed for three different assumed eruption times, 22:01 UTC on 7 August, 01:50 UTC and 04:35 UTC on 8 August, corresponding to the eruption times reported by AVO. For each inversion we assume that all $SO_2$ mass was emitted at one single eruption time. This is because we lack information on how much $SO_2$ was likely emitted during each eruption, and it is possible that most of the $SO_2$ was actually emitted during a single eruption. This approximation may yield inaccuracies, however as the time intervals between the eruptions are not very long, and the ECMWF wind profiles at Kasatochi did not change much over the interval that the eruptions occurred, this approach is assumed valid. Furthermore we used two different meteorological input data sets from ECMWF and GFS, for driving the FLEXPART simulations used for the inversion.

Figure 4 shows the results from the inversions for the 22:01 UTC eruption time using satellite data from one instrument at a time, and using ECMWF data for the model simulation. Generally, the emission profiles show that the eruption of Kasatochi resulted in large emissions of $SO_2$ both in the middle and upper troposphere (5-10 km) as well as in the lower stratosphere (10-15 km), with two strong emission peaks at ~7 km and ~12 km. Smaller emissions are found up to ~20 km. The largest stratospheric peak extends up to about 15-17 km which corresponds to the reports from AVO indicating emissions up to 14.5 - 16.5 km. On average, ~50% of the total mass is injected above the thermal tropopause at 10 km.

The strength of the two largest emission peaks depends on the satellite data set used. The inversion with GOME-2 data (red line) gives the largest stratospheric peak, and also the largest total $SO_2$ mass (2.4 Tg). The OMI profile (green line) is similar but with reduced emission peaks and a total $SO_2$ mass of 1.1 Tg. The AIRS profile (blue line) with a total $SO_2$ mass of 1.5 Tg, shows a strong ~7 km emission peak, a smaller stratospheric peak around 12 km, and also more emissions above 15 km. The anomalous peaks below 4 km are probably due to the poor sensitivity of AIRS in the lower troposphere.

The total $SO_2$ mass derived from the different AIRS overpasses were strongly fluctuating, partly because there were only two AIRS overpasses which covered the whole plume. Only for the overpass on 9 August 23:53 UTC (see figure 3), was the total mass within the same range (~1 Tg) as the GOME-2 and OMI total masses. Therefore, inversions were performed also using this overpass only (turquoise line). This also demonstrates that even when only one satellite overpass is used, results can be in good agreement with profiles based on more satellite data.

Subsequently, inversions were performed for all the three satellite data sets combined, and also for each of the three eruption times and for each of the two meteorological input data types. To compare the performance of the various inversions, we calculated Pearson correlation coefficients between the observations and the *a posteriori* model values, and RMSE as summarized in Table 2. While correlation coefficients and RMSE are only two of many possibilities to quantitatively describe how well the observations can be fitted by the model using the inverted vertical emission profile, they provide a simple means to compare and rank the

various simulations. Notice that the sum of squared errors is also the largest term in the cost function used for the inversion. When using the AIRS data, the correlation is lower for the inversions using the whole AIRS satellite data set (values in brackets in Table 2) compared to inversions using only the 9 August AIRS overpass. Therefore, for AIRS we chose to use only the one overpass for the remainder of this study.

The bold values in Table 2 indicate the three eruption times for which each meteorological data set yielded the highest correlations and lowest RMSE: ECMWF data for 22:01 UTC, GFS data for 01:50 UTC and 04:35 UTC, respectively. It can also be seen that correlation coefficients tend to be lower when using data from all three instruments at the same time. This can be explained by the biases in the satellite data, which deteriorate correlations. Nevertheless, we expect that inverted profiles are most reliable when all data are used. Figure 5 shows the three best estimates of the inversion profiles based on all satellite data for each eruption time, 22:01 UTC (red line) using ECMWF data, and 01:50 UTC and 04:35 UTC using GFS data (green line and blue line, respectively). While the shape and magnitude of the strong stratospheric peak (~12 km) is very similar for all inversion experiments, the altitude of the tropospheric peak depends on the assumed eruption time. Overall, however, the emission profile is quite robust and does not depend strongly on the assumed eruption time. It also does not depend strongly on the choice of the meteorological input data used for driving FLEXPART. The total mass of $SO_2$ is 1.7±0.08Tg for all profiles, with 1±0.11 Tg stratospheric injection (>10km) and emission up to a maximum altitude of ~20 km.

519 In principle, we could set up the inversion such that the emissions are not only determined as a
520 function of altitude but also of time. However, since the three eruptions occurred during such a
521 short time interval and the inversion results are very similar, the emissions of the three eruptions
522 cannot be clearly separated by the inversion. Therefore, we chose the two profiles with highest
523 correlation, the "ALL 22:01 ECMWF" and "ALL 01:50 GFS", to define the average of these two
524 profiles as the so-called "reference" profile (thick black line in Fig. 5). This profile was
525 subsequently used to perform a long-range transport simulation by assigning the $SO_2$ emissions
526 to a time window from the first to the second eruption time.
527
528 In Fig. 6, results from some sensitivity experiments are shown. All profiles are for an assumed
529 01:50 UTC eruption time. The 01:50 UTC profile (thick green line) is the same as the result in
530 Fig. 5, repeated for comparison. The 01:50 UTC constant profile (blue line) shows the inversion
531 profile using a constant *a priori* in contrast to an *a priori* based on IASI estimates. The similarity
532 between these two profiles demonstrates that with a sufficiently large satellite data set the
533 inversion results are robust to changes in the *a priori*, as stated also by *Eckhardt et al.* [2008].
534 The 01:50 UTC ECMWF profile (turquoise line) is the inversion result when using ECMWF
535 instead of GFS meteorological data for driving the FLEXPART simulations used for the
536 inversion, which result in somewhat lower correlation (0.60 vs. 0.62) for this eruption time. The
537 lower altitude emission peak is located higher than for the GFS results, which is generally the
538 case for the ECMWF results for all eruption times.
539
540 The figure also shows the ECMWF temperature profile (dark grey line) for the nearest grid point
541 (52°N, 176°W) to the volcano, as well as the ECMWF tropopause height (light grey line) located

542 at 10 km. There are no emissions at the tropopause height. The high stratospheric emission peak
543 is collocated with a layer of enhanced stability in the atmospheric temperature profile, which is
544 associated with detrainment of air. In the troposphere, except for the lowest 2 km, there is no
545 layer with particularly large stability, so there does not seem to be a height where detrainment is
546 most likely to occur.
547
548 **6.3. Simulation and validation of the $SO_2$ transport**
549 The transport of the volcanic $SO_2$ plume was simulated with FLEXPART using emissions
550 according to the reference inversion profile shown in Fig. 5. Particles were released continuously
551 from 22:01 UTC on 7 August until 01:50 UTC on 8 August because the results presented in
552 section 6.2 did not allow unambiguous determination of a single most appropriate time. This
553 transport simulation was compared with independent satellite data; that is, measurements which
554 were not used for the inversion. Comparisons with lidar measurements were also performed to
555 evaluate the height of the simulated $SO_2$.
556
557 The long-range transport simulations were performed using both ECMWF data and GFS data.
558 Comparisons and validations showed better agreement when using ECMWF data for the
559 simulation, thus only the results using ECMWF data are shown in this section. The results using
560 GFS data are only described where they clearly differ from the ECMWF results.
561
562 **6.3.1. Comparison with independent satellite data**
563 Figure 7 shows the FLEXPART simulation using the reference emission profile from Fig. 5
564 compared with independent satellite data from AIRS on 11 August, OMI on 12 August and

GOME-2 on 13 August. The model results are shown as isolines, while the satellite data are in color shadings. To give a best comparison between the model results and satellite data, the FLEXPART results are weighted with the respective averaging kernel from Fig. 2.

On 11 August, four days after the eruption, the $SO_2$ cloud hit the coast of Alaska and the plume was split into two parts. One part was transported across northern Canada towards Greenland and the other part spread towards the southern Great Lakes. It was the efficient transport near the tropopause (~12km) by the jet stream that caused the fast movement of the plume across North America. An AIRS satellite overpass at 22:05 UTC captured one part of the $SO_2$ cloud, with the swath width boundaries of the overpass indicated with the grey box (Fig. 7, top panel). For areas covered by the AIRS observations there is very good agreement between the model simulation and the measurements. The shape of the plume is especially simulated very well with a distinct sharp bend at the plumes southern end, and the tails stretching northward and southward.

On the next day, 12 August, the main part of the $SO_2$ plume has drifted northeastwards and is located over western Canada. The front tail of the plume is transported by the jet stream towards Greenland. The OMI satellite observations are composites of data collected for various moments during the day, while the FLEXPART results show the dispersed $SO_2$ at 21:01-22:01 UTC. Despite the time differences there is good agreement between measurements and FLEXPART simulation. The shape of the main part of the plume as well as the southern tail over the Pacific Ocean is captured very well, while there are some observations near Hudson Bay in Canada that are not simulated as well by FLEXPART. However, the model simulation using GFS data shows a better comparison for the areas around Hudson Bay (not shown).

Six days after the eruption on 13 August, the front tail of the $SO_2$ cloud hit the Atlantic Ocean, while the main part is found over northern Canada. The GOME-2 observations, shown as composites of overpasses during the day and the FLEXPART results for 16:01-17:01 UTC are in good agreement. The main features of the plume are captured very well by the model. Especially the position of the maximum over Canada correlates very well with the measurements. The two tails of the plume stretching over U.S and Canada, and also the tail remaining over the Pacific Ocean have distinct limits that the model recaptures. However, it seems that the model overestimates the leading tail of the plume over Greenland, and also the westernmost part of the plume over Alaska.

Some of the minor discrepancies between the model and satellite data may be due to that $SO_2$ loss is only estimated by FLEXPART. The e-folding time for the loss of $SO_2$ in the model simulation is about 1 day in the boundary layer, about 20 days for the upper troposphere and 50 days for the stratosphere, which is in agreement with loss rates found in literature [e.g., *Bluth et al.,* 1997]. Thus, the loss of tropospheric $SO_2$ is to some extent important for validation about a week after the eruption, whereas stratospheric loss is very slow and nearly negligible.

606 **6.3.2. Comparison with space-based lidar measurements**

607 CALIPSO profiles of total attenuated backscatter at 532 nm and 1064 nm (level 1B data) are
608 compared with $SO_2$ concentrations simulated by FLEXPART to evaluate the altitude of the
609 simulated plume. The comparison is qualitative as we compare two different quantities:
610 concentration of $SO_2$ with backscatter from particulate matter (aerosols and clouds).
611
612 The comparisons between the model simulation and CALIPSO were done in an area where the
613 volcanic plume was observed by other satellite instruments (see Fig. 1 and Fig. 3) and where we
614 can be confident that the scattering particles are indeed of volcanic origin. In addition, at this
615 latitude some of the altitudes used for comparison (above 10-12 km) are seldom reached by other
616 type of aerosols or liquid water clouds, but there may be ice clouds.
617
618 Figure 8 shows the $SO_2$ plume simulated by FLEXPART on 8 August (~15 h after the eruption)
619 with the CALIPSO nadir track overlaid (upper panel). The simulated transport patterns agree
620 very well with the satellite observations in Fig. 1, which were used for the inversion. Layers of
621 enhanced attenuated backscatter are found between 5 km and 11 km (lower panel), while the
622 plume simulated by FLEXPART shows two $SO_2$ layers centered at 6-8 and 11-12 km, coinciding
623 with the two emission maxima of the reference profile (Fig. 5). Generally the simulated plume is
624 broader than the CALIPSO features.
625
626 The lowest part of the simulated plume (5-9 km) coincides very well with the CALIPSO
627 measurements, and especially the latitudinal tilting agrees very well. However, the CALIPSO
628 Level 2 data product classifies this area as clouds with some minor aerosol near 5 km. The

629 conversion from $SO_2$ to sulphate is on the order of a few days in the lower troposphere, which
630 may indicate that, at this early stage after the eruption, CALIPSO sees volcanic ash, or possibly a
631 mixture of ash, sulphate and cloud. Also the attenuated color ratio (1064nm/532nm) is high (1.4-
632 1.6) for this part of the plume, indicating large particles. As the volcanic ash and $SO_2$ traveled
633 together for at least 3 days (*Prata et al.* [2009]), the comparison with the CALIPSO features
634 seems reasonable.
635
636 For the tropopause region (~10 km), layers with enhanced backscatter are found mainly around
637 10 km, while the simulated plume is located at 11-12 km. CALIPSO's scene classification imply
638 mostly clouds, the minor 11-12 km feature between 49 and 52°N is classified as "stratospheric
639 feature". This feature shows a stronger signal at 532 nm, indicating smaller particles, thus may
640 be small sulphate particles starting to form from the $SO_2$. The dislocation between the observed
641 10 km layer and the simulated 12 km layer may be explained by the very slow conversion rate
642 from $SO_2$ to sulfate in the stratosphere, thus sulfate particles have not yet started to form. Or, if
643 the observed features at 10 km are volcanic ash particles, they may have subsided due to
644 gravitational settling. The depolarization ratio for the observations is 0.2 - 0.4. Interestingly, the
645 cirrus cloud (strong backscatter, higher depolarization of 0.4-0.5) at ~10 km and 54°N, is not
646 part of the simulated volcanic plume.
647
648 Figure 9 shows a similar comparison of the plume transport simulated by FLEXPART and the
649 CALIPSO measurements from 9 August (~48 h after the eruption). Visually the transport
650 patterns agree with the satellite observations in Fig. 3, also used for the inversion. The CALIPSO
651 track cuts through the plume's tail at around 162 °W. The enhanced backscatter at 1064 nm is

652 shown as some of the observed features were more clearly visible at this wavelength rather than
653 at 532 nm. Three thin veils of enhanced backscatter are observed between 43-47°N at ~3 km,
654 ~12 km and ~15 km altitude. The FLEXPART model results show similar layers centered at the
655 same altitudes, but the highest layer is covering a broader vertical range, the middle layer is
656 narrower and the lowest layer is broader and extending further north. For the lowest layer it is the
657 bottom part of the maximum that corresponds to the CALIPSO feature. The two highest
658 CALIPSO layers are characterized as stratospheric features, while the lowest layer is a mixture
659 of aerosol and cloud. The stratospheric layer has depolarization ratio around 0.1-0.2 and color
660 ratio <1, indicating a potential mixture of sulphate aerosols and other volcanic debris. Both the
661 depolarization ratio and the color ratio are highest for the layer in the lower troposphere,
662 indicating larger particles, thus maybe volcanic ash. The larger extent of the $SO_2$ layer compared
663 to the area with enhanced backscatter can be due to wash out of the sulfate particles and ash at
664 this low altitude. Overall, the approximate plume position and especially the three-layer structure
665 and the three layers' mean altitudes are well captured.
666

667 **6.3.3. Comparison with ground-based lidar measurements**

668 To further validate the height of the simulated plume, we used ground-based lidar measurements
669 at two different locations. These lidar observations were taken from 8 to 25 days after the
670 eruption, on a location over 100° east of the volcano. Since the ash from the eruption was likely
671 deposited after a few days, the observations that can be related to the eruption are of sulphate
672 aerosols converted from the $SO_2$ emissions.

673

674 The Kasatochi plume was observed by the Dalhousie Raman lidar at Nova Scotia (44.6°N,
675 63.6°W) on the eastern coast of Canada. The measurements of the plume were available from 14
676 August 2008 on certain days until the end of October.

677

678 Fig. 10 shows the FLEXPART $SO_2$ plume on 18 August and lidar measurements from 18-19
679 August with corresponding FLEXPART isolines overlaid. The lidar position is marked with a
680 green dot. The $SO_2$ plume is found mostly over Northern U.S., Canada, over western Alaska and
681 over Greenland, and there is also debris over Nova Scotia. The aerosol extinction coefficients
682 indicate an aerosol layer at ~14-15 km altitude, which corresponds very well with the $SO_2$ layer
683 simulated by FLEXPART, but the measured aerosol plume is narrower in its vertical extent than
684 the simulated $SO_2$ cloud. Also the maximum $SO_2$ concentration at around 03:00 UTC on 18
685 August is located slightly higher than the maximum aerosol concentration.

686

687 Fig. 11 shows the simulated $SO_2$ plume and lidar measurements from 21-22 August. The $SO_2$
688 plume is still visible over Nova Scotia, and an observed layer at ~18 km fits very well with the
689 simulated plume to within ±0.5 km. This coincides with the minor emission peak at ~18km of

690 our reference emission height profile, and thus the lidar measurements provide validation that the
691 emissions from Kasatochi reached at least 18-20 km altitude.
692
693 Observations of the Kasatochi plume were also performed using a ground based lidar at
694 AWIPEV station, in Ny Ålesund (78.9°N, 11.9°E) on Svalbard. The lidar measurements of the
695 Kasatochi plume were taken from 15 August 2008 to 24 September 2008. Several layers were
696 observed at about 10-12 km and 15-17 km altitude [*Hoffmann et al.*, 2009].
697
698 Fig. 12 shows the simulated $SO_2$ plume and lidar measurements from 15 August with
699 FLEXPART isolines overlaid. The $SO_2$ plume has stretched out from Alaska all the way to
700 Europe. From the model simulation a thin tail of the plume has reached the lidar on Svalbard
701 (green dot), and small amounts (0.5-2.0 $\mu$g $m^{-3}$) of $SO_2$ are found at an altitude of 8-10 km above
702 Ny Ålesund. This is indicated in the lower panel and is in agreement with high aerosol
703 backscatter coefficients at this altitude. The lidar observations also show an aerosol layer at ~11
704 km altitude which is not found in the model simulation. Only for the observations after 25
705 August, is this layer present in the model simulation, as shown in Fig. 13 for 1 September. For
706 this day, there is also a very weak aerosol layer observed at 17 km which is also visible in the
707 model simulation. The lidar measurements from 1 September have been examined in detail by
708 *Hoffmann et al.* [2009].
709
710 Generally, the altitude of the simulated plume agrees very well with the different lidar
711 observations, but the modeled plume is generally broader than the measured aerosol plume in its
712 vertical extent.
713

## 7. Summary and conclusions

An inversion method was used in this study to estimate the vertical profile of $SO_2$ emissions from the eruption of Kasatochi Volcano in August 2008. This was done by using total column measurements of $SO_2$ from satellite instruments (GOME-2, OMI and AIRS) and a Lagrangian dispersion model, FLEXPART. Conclusions from this study are summarized as follows:

1. Emission height profiles of $SO_2$ were estimated by using $SO_2$ column data from GOME-2, OMI and AIRS for two days after the eruption. Two meteorological data sets (ECMWF and GFS) and three different eruption times were tested; 22:01 UTC on 7 August, 01:50 UTC and 04:35 UTC on 8 August. The first two eruption times yielded the highest correlation between measurements and model results. Generally, two large emission maxima were found; one in the stratosphere (~12 km a.g.l), and one in the middle-upper troposphere (~7km). The largest emission peak extended up to ~17 km which agreed with reports from AVO stating emissions up to 14.5-16.5 km a.s.l., but smaller emissions were obtained for up to ~20 km. According to the "reference" inversion (using satellite data from all three platforms), approximately 1.7±0.08 Tg $SO_2$ were emitted to the atmosphere, of which ~60% were injected above the tropopause located at 10 km. The estimated emission height profiles showed good agreement with height emission profiles from independent studies, such as estimates based on a trajectory ensemble technique [*Maerker et al.*, 2008], and also *Theys et al.* [2009].

2. The long-range dispersion of the $SO_2$ plume was simulated by FLEXPART using emissions according to our best-guess "reference" inversion profile. The plume spread mainly southeastward from the volcano and took on a circular shape due to a passing cyclone. The

plume was further transported towards the coast of Alaska where it split into two and traversed the North American continent in two ”tails” before reaching the Atlantic Ocean and Europe within a week after the eruption. The simulated plume was compared to independent satellite data up to six days after the eruption. There was overall good agreement between the simulated plume and the observations.

3. The height of the simulated plume was evaluated in a qualitative manner using lidar measurements. Compared to CALIPSO measurements on 8 and 9 August, one and two days after the eruption, the height of the simulated plume agrees very well. In particular, three separate layers were identified at altitudes within ~1 km of the altitudes of the observed layers. Compared to observations from Nova Scotia 10-15 days after the eruption the height of the modeled plume agreed with the observations to within ~1 km, and the comparison also demonstrated that $SO_2$ was injected to an altitude of 18-20 km by the volcanic eruption. The model results also agreed with observations on Svalbard 8-25 days after the eruption.

Challenges and restrictions of this case study include the following:
The eruption of Kasatochi was characterized by three different eruption times and also subsequent continuous release, and there was no information on how much $SO_2$ was released during each eruption. The eruptions were not clearly separable by our method, thus we made the assumption that all $SO_2$ mass was emitted at once, using a time window between the best-fitting eruption times. Furthermore, the first satellite detection of the plume by AIRS, GOME-2 and OMI was about 16, 23, 25 hours after the first eruption, which makes it difficult to demonstrate a near-real time application for this case study.

760

761 The inversion method presented here can provide information needed in order to calculate the
762 actual and future position and extent of volcanic plumes. This information can be utilised in near
763 real-time applications by e.g., the VAACs to rapidly issue warnings on volcanic ash hazards. As
764 soon as satellite data are available for the eruption, the inversion method can be applied and the
765 results can be ready within minutes to a few hours. The method presented can also be utilised for
766 less time-critical studies, such as facilitating the understanding of the climatic impacts of
767 stratospheric $SO_2$.

768

769 **Acknowledgments.** The authors are grateful to the European Space Agency for funding this
770 study through the SAVAA project and especially to Dr Claus Zehner. We thank I. Bey for
771 supplying us with OH fields from GOES-CHEM. We acknowledge ECMWF and the Norwegian
772 Meteorological Institute for providing access to the ECMWF archives. CALIOP data were
773 obtained from the NASA Langley Research Center Atmospheric Science Data Center. We are
774 also grateful to the KNMI and NASA science and data distribution teams for use of the AIRS,
775 GOME-2 and OMI data. We would like to thank N. Krotkov and K. Yang at GEST for useful
776 information on the OMI retrievals for Kasatochi. Harald Sodemann at NILU is acknowledged for
777 retrieving nested ECMWF data.

## References


Alaska Volcano Observatory (2008), Alaska Volcano Observatory, Kasatochi Eruption Page, *http://www.avo.alaska.edu/activity/Kasatochi.php*

Bey, I., D. J. Jacob, R. M. Yantosca, J. A. Logan, B. D. Field et al. (2001), Global modeling of tropospheric chemistry with assimilated meteorology: Model description and evaluation, *J. Geophys. Res., 106*(D19), 23073–23096, doi:10.1029/2001JD000807.

Bitar, L., T. J. Duck, N. Kristiansen, A. Stohl, N. Bousserez, C. Lee, A. van Donkelaar, R. V. Martin, S. Beauchamp (2009), Lidar observations of Kasatochi volcano aerosols in the troposphere and stratosphere, *J. Geophys. Res.*, Special issue "The 2008 eruptions of Okmok and Kasatochi volcanoes, Alaska", to be published.

Bluth, G.J.S., W.I. Rose, I.E. Sprod and A.J. Krueger (1997), Stratospheric loading of sulfur from explosive volcanic eruptions, The Journal of Geology, 105, pp. 671-683.

Carn, S. A., A. J. Krueger, N. A. Krotkov, K. Yang, and K. Evans (2008), Tracking volcanic sulfur dioxide clouds for aviation hazard mitigation, *Nat. Hazards.,* doi:10.1007/s11069-008-9228-4.

Chahine, M., et al. (2006), AIRS: Improving Weather Forecasting and Providing New Data on Greenhouse Gases, *Bull. Am. Meteorol. Soc., 87*(7), pp. 911–926, doi:10.1175/BAMS-87-7-911.

Eckhardt, S., A. J. Prata, P. Seibert, K. Stebel, and A. Stohl (2008), Estimation of the vertical profile of sulfur dioxide injection into the atmosphere by a volcanic eruption using satellite column measurements and inverse transport modeling, *Atmos. Chem. Phys., 8*, pp. 3881–3897.

ECMWF (2002), Edited by: P. W. White, P.W.: IFS Documentation, *ECMWF*, Reading, UK, available at: http://www.ecmwf.int.

Emanuel, K. A., and M. Živković-Rothman (1999), Development and evaluation of a convection scheme for use in climate models, *J. Atmos. Sci., 56*, pp. 1766–1782.

Forster, C., A. Stohl, and P. Seibert (2007), Parameterization of convective transport in a Lagrangian particle dispersion model and its evaluation, *J. Appl. Met. Clim., 46*(4), pp. 403–422, doi: 10.1175/JAM2470.1.

Halmer, M. M., and H.-U. Schmincke (2003), The impact of moderate-scale explosive eruptions on stratospheric gas injections, *Bull. Volcanol., 65*(6), pp. 433–440, doi: 10.1007/s00445-002-0270-x.

Hoffmann, A., C. Ritter, M. Stock, M. Maturilli and R. Neuber (2009), Lidar measurements of the Kasatochi aerosol plume in August and September 2008 in Ny-Ålesund, Spitsbergen, *J. Geophys. Res.,* Special issue "The 2008 eruptions of Okmok and Kasatochi volcanoes, Alaska", to be published.

Hostetler, C. A., Z. Liu, J. Reagan, M. Vaughan, M. Osborn, W.H. Hunt, K.A. Powell, and C. Trepte (2006), CALIOP Algorithm Theoretical Basis Document, Calibration and Level 1 Data Products, PC-SCI-201, NASA Langley Res. Cent., Hampton, Va., Available at http://www-calipso.larc.nasa.gov/resources/project_documentation.php

Jäger, H., and T. Deshler (2002), Lidar backscatter to extinction, mass and area conversions for stratospheric aerosols based on midlatitude balloonborne size distribution measurements, *Geophys. Res. Lett., 29*(19), 1929, doi:10.1029/2002GL015609.

821 Karagulian, F., L. Clarisse, P. F. Coheur, A.J. Prata, D. Hurtmans, and C. Clerbaux (2009),
822 Detection of SO2, ash and H2SO4 using the IASI sounder, *J. Geophys. Res.*, to be
823 published.
824 Klett, J. (1981), Stable analytical inversion solution for processing lidar returns, *Appl. Opt.,*
825 *20*(2), pp. 211-220. doi:10.1364/AO.20.000211
826 Kristiansen, N. I. (2009), Determination of the emission height profile of volcanic emissions
827 using inverse modeling, M.S. thesis in Geosciences, Meteorology, 82 pp, Univ. of Oslo,
828 Norway,
829 http://www.duo.uio.no/publ/geofag/2009/90532/MasterThesis_NinaIrenKristiansen.pdf
830 Krotkov, N. A., S. A. Carn, A. J. Krueger, P. K. Bhartia, and K. Yang (2006), Band Residual
831 Difference Algorithm for Retrieval of SO2 From the AURA Ozone Monitoring
832 Instrument (OMI), *IEEE Trans. Geosci. and Remote Sens., 44*(5), pp. 1259–1266, doi:
833 10.1109/TGRS.2005.861932.
834 Maerker, K. C., P. V. Rix, and J. Van Geffen (2008), Trajectory matching and dispersion
835 modeling of volcanic plumes utilizing space-based observations, In: *Proceedings of the*
836 *2008 second workshop on USE of Remote Sensing Techniques for Monitoring Volcanoes*
837 *and Seismogenic Areas USEReST* 2008, 11-14 Nov. 2008, Naples, Italy, IEEE
838 publication.
839 Mankin, W. G., M. T. Coffey, and A. Goldman (1992), Airborne observations of $SO_2$, HCl, and
840 $O_3$, in the stratospheric plume of the Pinatubo volcano in July 1991, *Geophys. Res. Lett.,*
841 *19*(2)*,* 179–182.
842 McCormick, M. P., L. W. Thomason, and C. R. Trepte (1995), Atmospheric effects of the Mt.
843 Pinatubo eruption, *Nature, 373*, 399–404, doi: 10.1038/373399a0.

844 Menke, W. (1984), *Geophysical Data Analysis: Discrete Inverse Theory*, 260 pp.,
845 Academic Press, Orlando, USA,
846 Munro, R., et al. (2006), GOME-2 on MetOp, *paper presented at the 2006 EUMETSAT*
847 *Meteorological Satellite Conference*, EUMETSAT, Helsinki,12- 16 June.
848 NASA (2008), Volcanoes, Aleutian Islands' Kasatochi Volcano Eruption Pages. *NASA's Earth*
849 *Observatory and Natural Hazards*, http://earthobservatory.nasa.gov/NaturalHazards/.
850 Oberhuber, J. M., M. Herzog, H.-F. Graf and K. Schwanke (1998), Volcanic plume simulation
851 on large scales, *J. Volcan. Geoth. Res., 87*(1-4), pp. 29–53.
852 O'Malley, J. and B. Bragg (2008), Planes flying again after ash cancellations, *Anchorage Daily*
853 *News*. Published August 11th, 2008, http://www.adn.com/news/alaska/story/490210.html.
854 Prata, A. J., S. A. Carn, A. Stohl, and J. Kerkmann (2007), Long range transport and fate of a
855 stratospheric volcanic cloud from Soufrière Hills volcano, Montserrat, *Atmos. Chem.*
856 *Phys., 7*(19), pp. 5093–5103.
857 Prata, A. J. and C. Bernardo (2007), Retrieval of volcanic $SO_2$ column abundance from
858 Atmospheric Infrared Sounder data, *J. Geophys. Res., 112*, D20204,
859 doi:10.1029/2006JD007955.
860 Prata, A. J., G. Gangale, L. Clarisse,and F. Karagulian (2009), Ash and sulphur dioxide in the
861 2008 eruptions of Okmok and Kasatochi - insights from high spectral resolution satellite
862 measurements. *J. Geophys. Res*., Special issue "The 2008 eruptions of Okmok and
863 Kasatochi volcanoes, Alaska", to be published.
864 Richter, A., F. Wittrock, and J. P. Burrows (2006), $SO_2$ measurements with SCIAMACHY, in
865 Proceedings of the First Conference on Atmospheric Science, SP-628, ESA, Frascati,
866 Italy, May 2006.

867 Richter, A., F. Wittrock, A. Schönhardt, and J. P. Burrows (2009a), Quantifying volcanic $SO_2$
868 emissions using GOME-2 measurements, *poster presented at European Geosciences*
869 *Union General Assembly, Vienna, Austria, April 2009*, EGU2009-7679 AS3.15 XY247.
870 Richter, A. F. (2009b), GOME-2 volcanic $SO_2$ Algorithm Theoretical Basis Document.
871 Available from the SAVAA project documentation.
872 Rix, M., P. Valks, N. Hao, T. Erbertseder, and J. van Geffen (2008), Monitoring of volcanic
873 SO2 emissions using the GOME-2 satellite instrument, In: *Proceedings of the 2008*
874 *second workshop on USE of Remote Sensing Techniques for Monitoring Volcanoes and*
875 *Seismogenic Areas USEReST* 2008, 11-14 Nov. 2008, Naples, Italy, IEEE publication.
876 Rodgers, C. D. (2000), *Inverse Methods for Atmospheric Soundings: Theory and Practice*, 238
877 pp., World Sci., Singapore.
878 Seibert, P. (2000), Inverse modelling of sulfur emissions in Europe based on trajectories, In:
879 *Inverse Methods in Global Biogeochemical Cycles*, Vol. 114, edited by P. Kasibhatla et
880 al., pp. 147-154, AGU Geophysical Monograph Series.
881 Smithsonian Institution (2008), Global Volcanism Program, http://www.volcano.si.edu/
882 Stohl, A., M. Hittenberger, and G. Wotawa (1998), Validation of the Lagrangian Particle
883 Dispersion model FLEXPART against large-scale tracer experiment data, *Atmos.*
884 *Environ., 32*(24), pp. 4245–4264, doi:10.1016/S1352-2310(98)00184-8
885 Stohl, A. and D. J. Thompson (1999), A density correction for Lagrangian particle dispersion
886 models, *Boundary-Layer Meteorol., 90*(1), pp. 155–167, doi:10.1023/A:1001741110696.
887 Stohl, A., C. Forster, A. Frank, P. Seibert, and G. Wotawa (2005), Technical note: The
888 Lagrangian particle dispersion model FLEXPART version 6.2, *Atmos. Chem. Phys., 5*(9),
889 pp. 2461–2474.

Textor, C., H.-F. Graf, M. Herzog, and J. M. Oberhuber (2003), Injection of gases into the stratosphere by explosive volcanic eruptions, *J. Geophys. Res., 108*(D19), 4606, doi:10.1029/2002JD002987.

Theys, N., M. van Roozendael, B. Dils, F. Hendrick, N. Hao, and M. De Maziere (2009), First satellite detection of volcanic bromine monoxide emission after the Kasatochi eruption, *Geophys. Res. Lett., 36*, L03809, doi:10.1029/2008GL036552.

VAAC (2008), Volcanic Ash Advisory Centers, http://www.metoffice.gov.uk/aviation/vaac/

Wang, X., A. Boselli, L. D'Avino, G. Pisani, N. Spinelli et al. (2008), Volcanic dust characterization by EARLINET during Etna's eruptions in 2001-2002, *Atmos. Environ., 42*, pp. 893–905.

Waythomas, C.F., S. G. Prejean and D. J. Schneider (2008), Small volcano, big eruption, scientists rescued just in time, *US Department of the Interior online publication People, Land, and Water preprint.*, http://www.avo.alaska.edu/activity/Kasatochi08/Kasatochi2008PLW.php

Wesely, M. L. (1989), Parameterization of surface resistances to gaseous dry deposition in regional-scale numerical models, *Atmos. Environ, 23*, pp. 1293–1304. doi:10.1016/j.atmosenv.2007.10.058.

Wesely, M.L., and B. B. Hicks (1977), Some factors that affect the deposition rates of sulfur dioxide and similar gases on vegetation, *J. Air Poll. Contr. Assoc., 27*, pp. 1110–1116.

Yang, K., N. A. Krotkov, A. J. Krueger, S. A. Carn and P. K. Bhartia (2007), Retrieval of large volcanic SO2 columns from the Aura Ozone Monitoring Instrument: Comparison and limitations, *J. Geophys. Res., 112*, D24S43, doi: 10.1029/2007JD008825.

| **Satellite retrieval** | **Total mass $SO_2$** | **Reference** |
|---|---|---|
| GOME-2 | ~2.5 Tg | *Richter et al.* [2009a] |
| OMI | ~1.4 Tg | *NASA* [2008] |
| AIRS | ~1.2 Tg | *Prata* [2009] (this issue)<br>This paper |
| IASI | ~2.2 Tg | *Karagulian et al.* [2009] |

**Table 1:** Estimates of total $SO_2$ mass emitted by the eruption of Kasatochi, for different satellite retrievals.

| Model Input data | Satellite data | ERUPTION TIMES | | | | | |
|---|---|---|---|---|---|---|---|
| | | **22:01 UTC** | | **01:50 UTC** | | **04:35 UTC** | |
| | | **r** | **RMSE** | **r** | **RMSE** | **r** | **RMSE** |
| ECMWF | GOME-2 | 0.65 | 2.72 | 0.62 | 2.94 | 0.59 | 3.09 |
| | OMI | 0.64 | 1.02 | 0.63 | 1.08 | 0.60 | 1.17 |
| | AIRS | 0.69 (0.31) | 0.72 (0.96) | 0.65 (0.28) | 0.80 (1.01) | 0.62 (0.21) | 0.84 (1.08) |
| | ALL | **0.62** (0.41) | **1.93 (**2.04) | 0.60 (0.41) | 2.07 (2.13) | 0.56 (0.37) | 2.22 (2.26) |
| GFS | GOME-2 | 0.61 | 2.82 | 0.69 | 2.74 | 0.67 | 2.97 |
| | OMI | 0.62 | 1.03 | 0.69 | 0.98 | 0.69 | 1.01 |
| | AIRS | 0.66 (0.42) | 0.77 (0.91) | 0.56 (0.32) | 0.88 (0.99) | 0.55 (0.30) | 0.90 (1.04) |
| | ALL | 0.57 (0.46) | 1.98 (1.98) | **0.62** (0.42) | **1.99** (2.08) | **0.60** (0.45) | **2.07** (2.16) |

**Table 2:** Summary of all inversions performed (using different meteorological input data, different satellite data and three eruption times) and corresponding Pearson correlation coefficients (r) between the observations and the *a posteriori* model values, and root mean square errors (RMSE) given as E-03 $kgm^{-2}$. Values in brackets are indicating the inversions using the whole AIRS satellite data set in contrast to using only one AIRS overpass on 9 August. The bold values indicate the three eruption times for which each meteorological data set yielded the highest correlations and lowest RMSE.

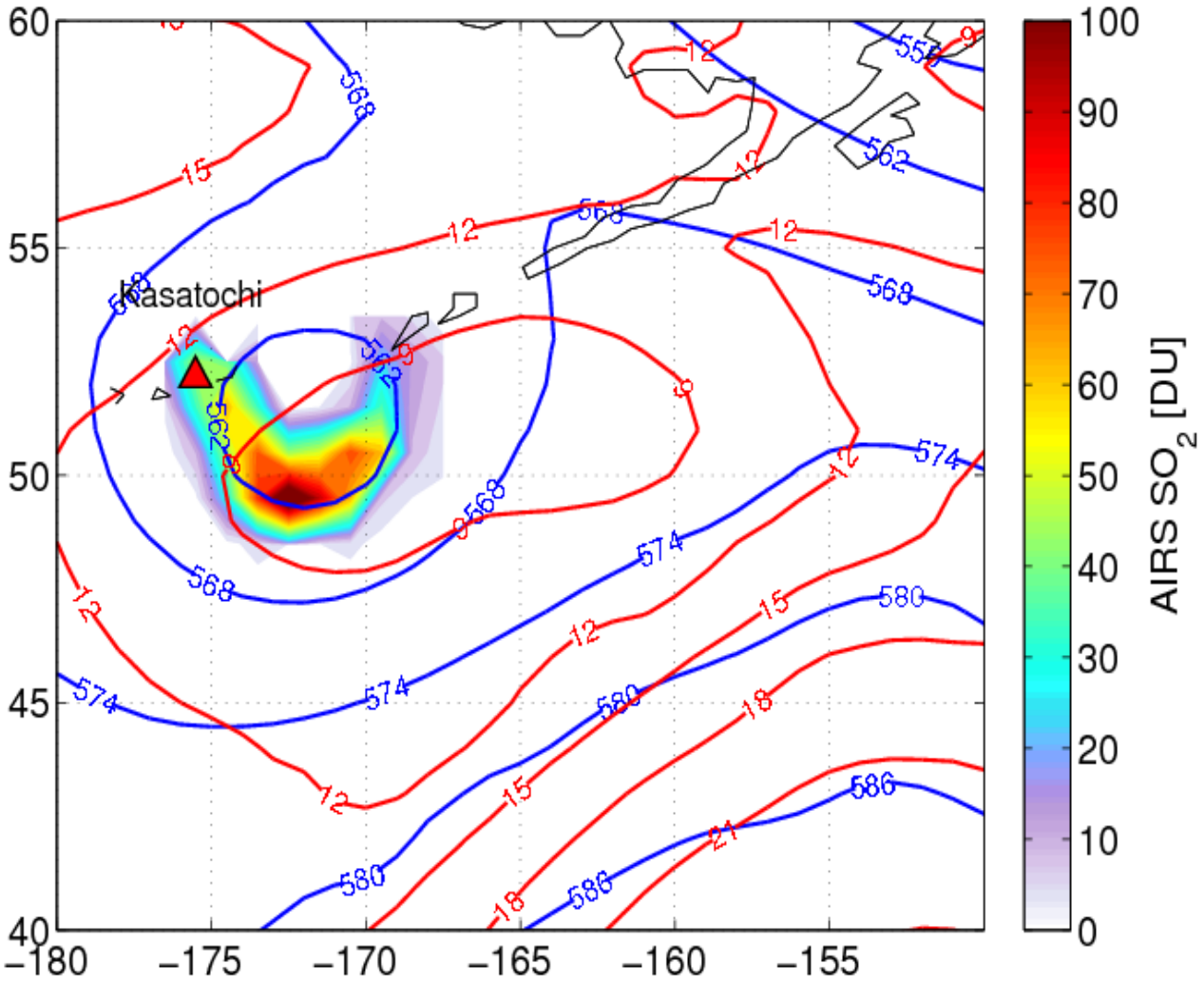


928

929 **Figure 1:** Geopotential height [$10^1$ m] in the area of the Kasatochi Volcano, on pressure levels
930 1000 hPa (red lines) and 500 hPa (blue lines) from the ECMWF analysis, on 8 August 2008 at
931 12:00 UTC. Satellite measurements of $SO_2$ total columns by AIRS on 8 Aug 13:41 UTC are
932 shown in color shadings. The Kasatochi Volcano is marked by a red triangle.

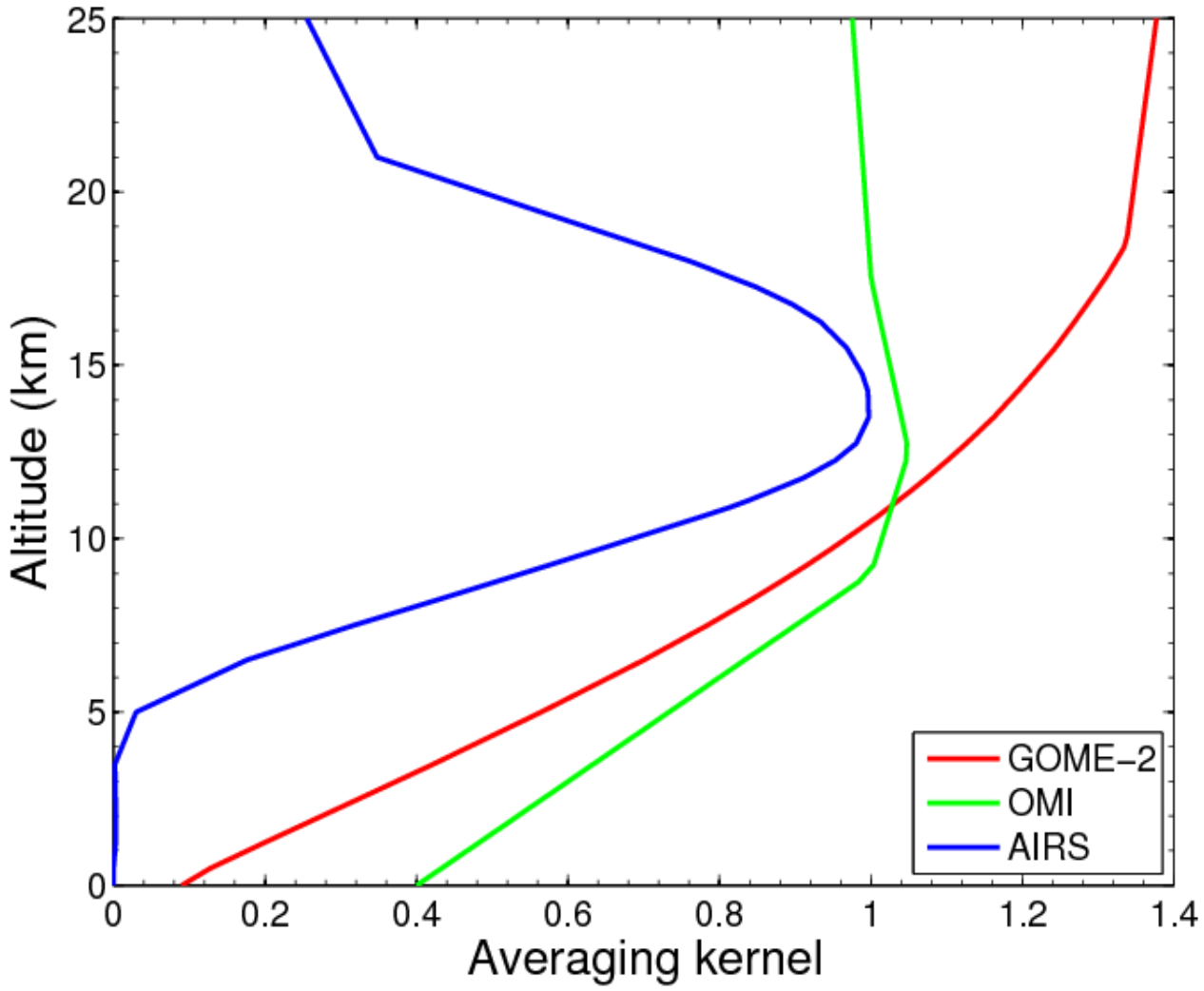


933

934 **Figure 2:** Averaging kernels for the GOME-2, OMI and AIRS retrievals of $SO_2$.

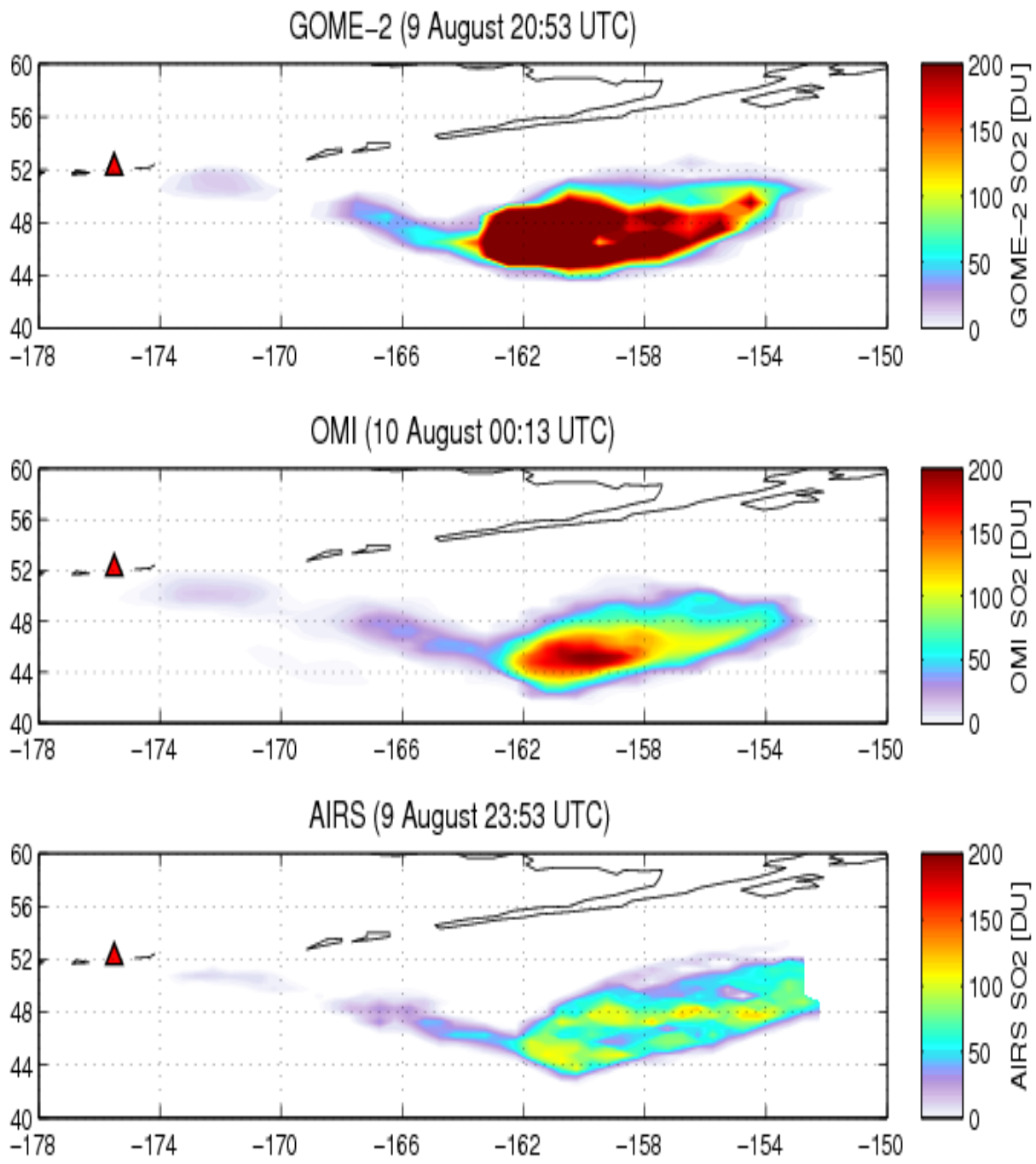


935

936 **Figure 3:** $SO_2$ columns retrieved from GOME-2, OMI and AIRS measurements on 9-10 August

937 2008. The Kasatochi Volcano is marked by a red triangle.

938

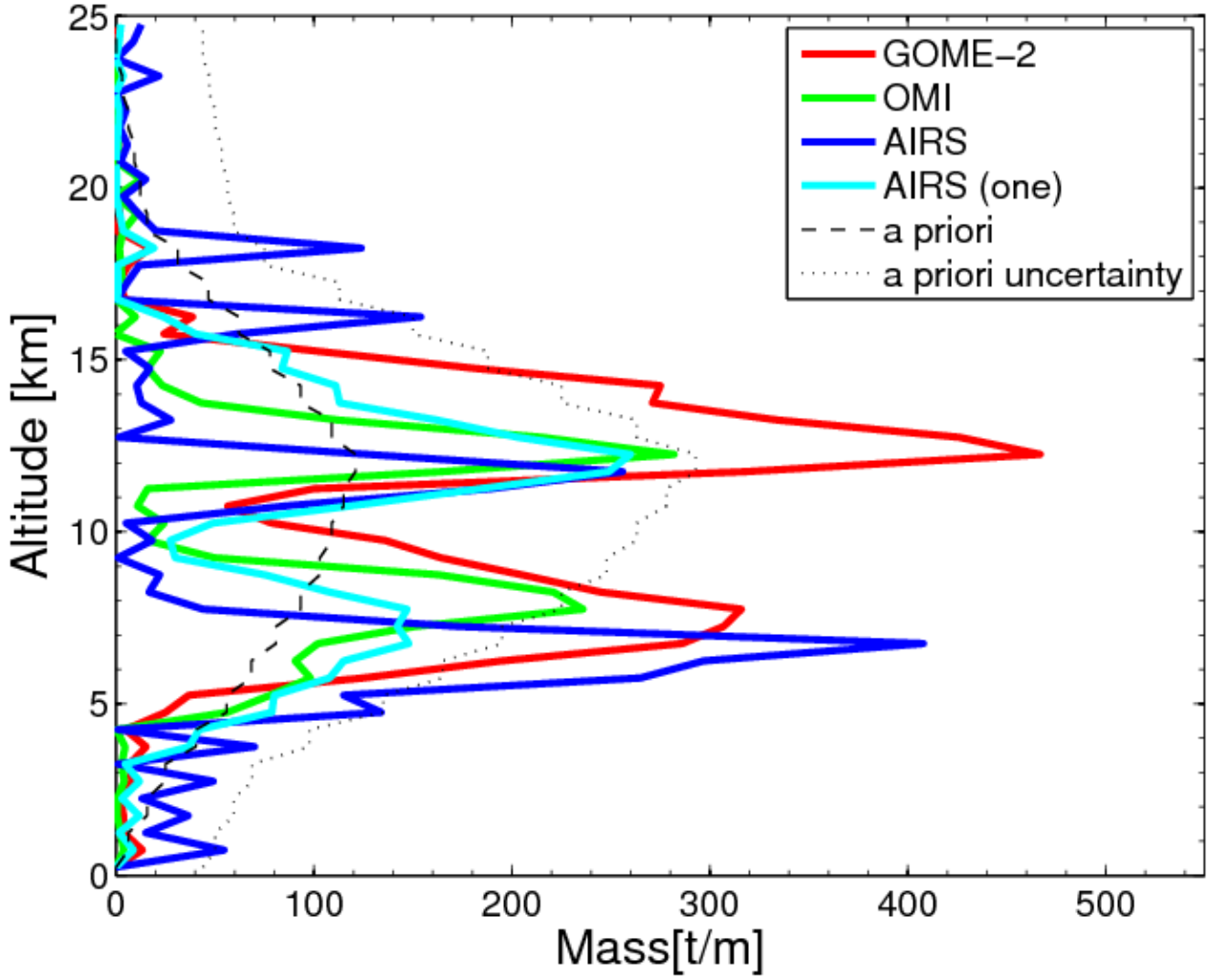


939

940 **Figure 4:** Inversion results for the 22:01 UTC assumed eruption time using satellite data from
941 one instrument at the time; GOME-2 (red line), OMI (green line) and AIRS (blue line). The
942 AIRS (one) profile is the inversion result when using only one AIRS satellite overpass on 9
943 August at 23:53 UTC. ECMWF meteorological data were used for driving the FLEXPART
944 simulations used for these inversions.

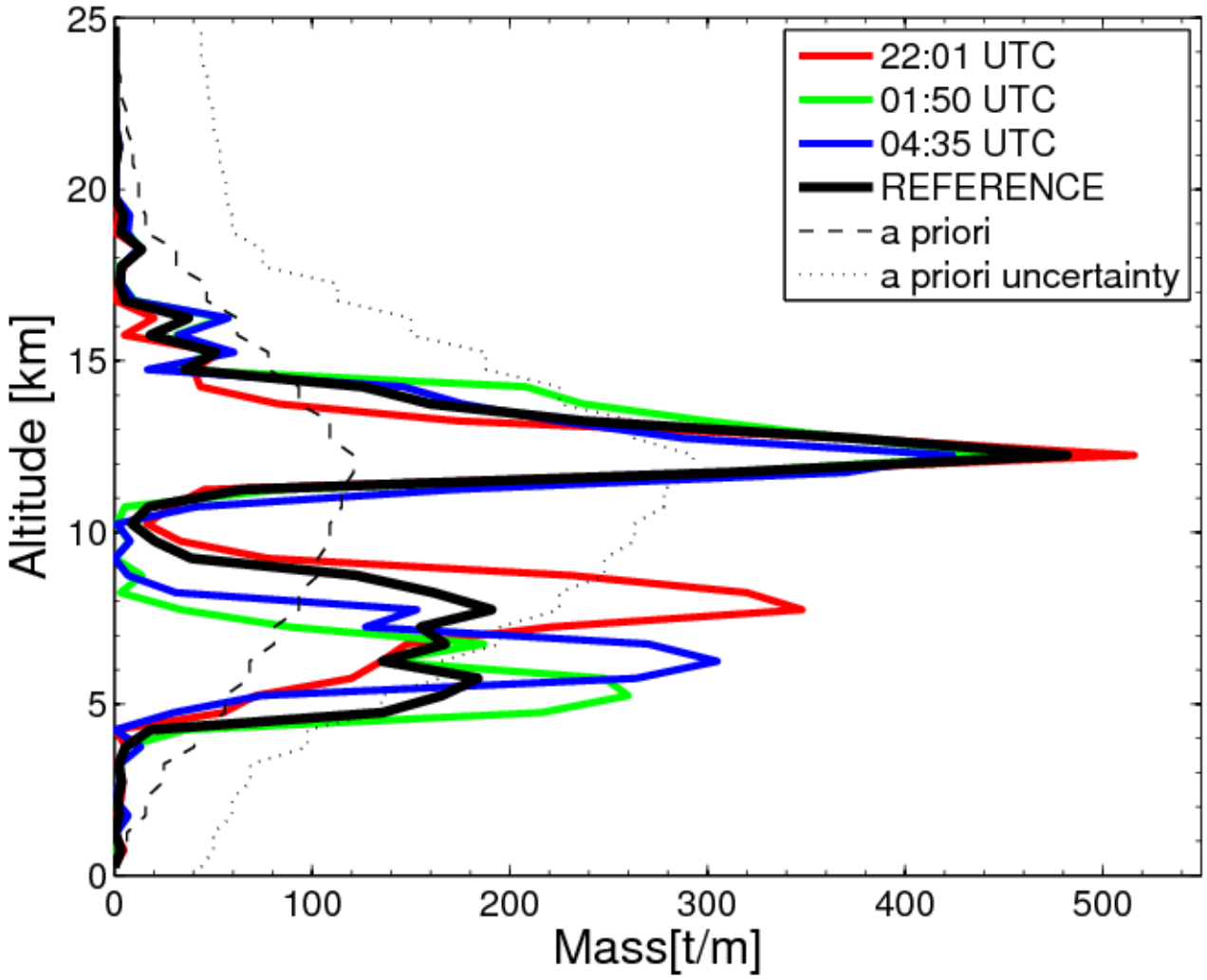


945

946 **Figure 5:** Inversion results when using combined satellite data from all three platforms (GOME-
947 2, OMI and AIRS) for three different assumed eruption times: 22:01 UTC on 7 August (red line),
948 01:50 UTC (green line) and 04:35 UTC on 8 August (blue line). The reference profile (thick
949 black line) is the average of the 22:01 UTC and the 01:50 UTC profiles. The ECMWF
950 meteorological data set were used for driving the FLEXPART simulations used for the 22:01
951 UTC inversion, while for 01:50 UTC and 04:35 UTC the GFS data were used.

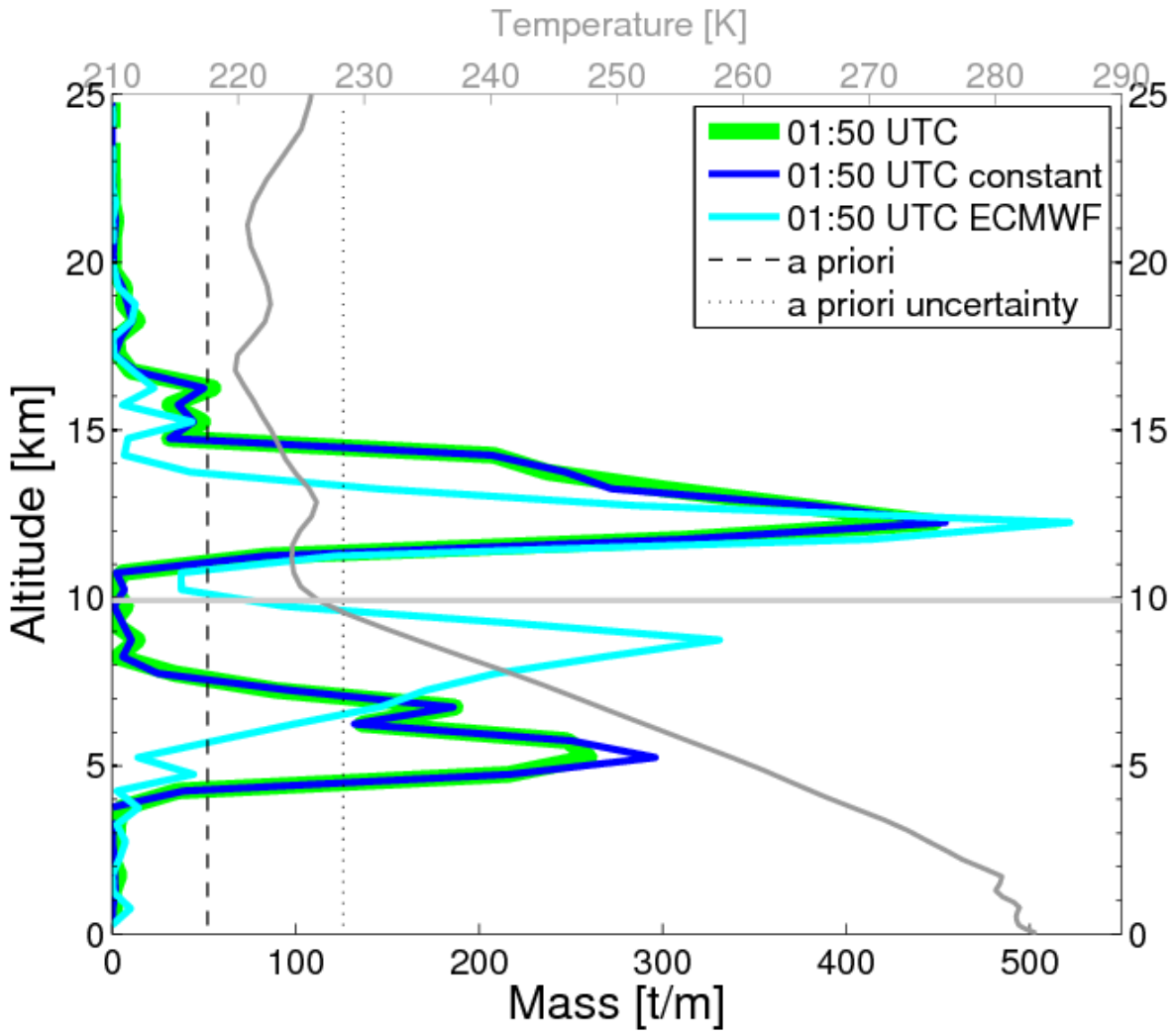


952

953 **Figure 6:** Sensitivity experiments with the inversion algorithm. The profile 01:50 UTC (green
954 line) is the same result as shown in figure 5. The profile 01:50 UTC constant (blue line) is using
955 constant *a priori* emissions (flat *a priori* profile). The profile 01:50 UTC ECMWF (turquoise
956 line) is the inversion result when using ECMWF meteorological data for driving the FLEXPART
957 simulations used for the inversion, instead of using GFS data. The dark grey line is the ECMWF
958 temperature profile for (52°N, 176°W) at 00:00 UTC on 8 August. The tropopause diagnosed
959 from ECMWF data is located at 10 km (light grey line).

960

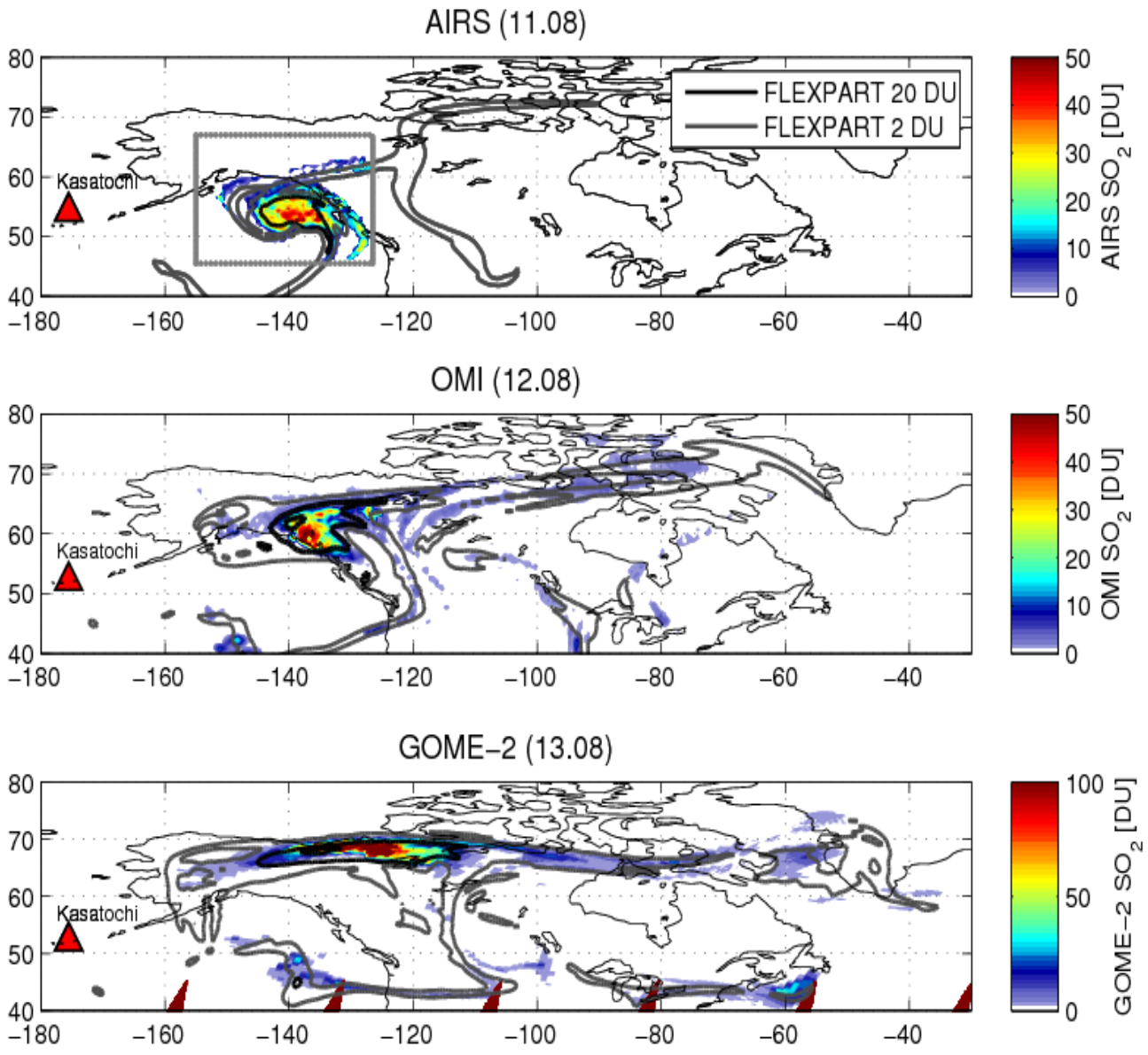


961

962 **Figure 7:** Comparison of $SO_2$ columns measured by satellite and simulated by FLEXPART
963 using the emission profile from the reference inversion. Satellite data (AIRS for 11 August, OMI
964 for 12 August and GOME-2 for 13 August 2008) are shown by the color shadings, and the
965 FLEXPART results, driven with ECMWF data, are shown as isolines for 2 DU (thick grey line)
966 and 20 DU (thick black line). For AIRS, the satellite's approximate swath width boundaries are
967 shown by grey dotted lines. The Kasatochi Volcano is marked by a red triangle.

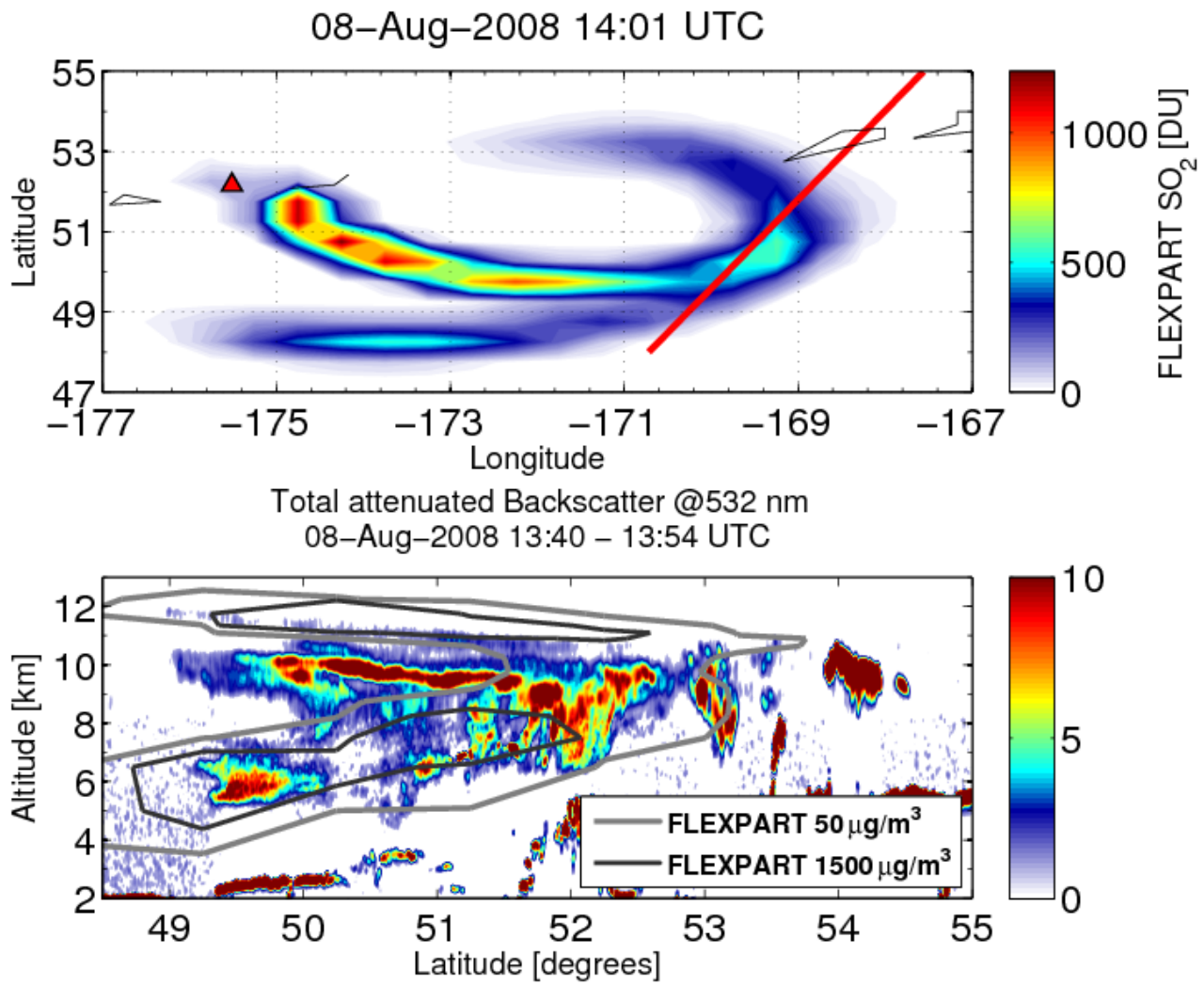


968

969 **Figure 8:** Comparison of CALIPSO attenuated backscatter at 532 nm with $SO_2$ concentrations
970 simulated by FLEXPART on 8 August. The upper panel shows total columns of $SO_2$ simulated
971 by FLEXPART. The red line indicates the location of the CALIPSO nadir track. In the lower
972 panel, CALIPSO data are shown by the color shadings (in $10^{-3}$ /m sr) and the FLEXPART results
973 are plotted as isolines for 50 $\mu g$ $m^{-3}$ (thick grey line) and 1500 $\mu g$ $m^{-3}$ (thick black line).

974

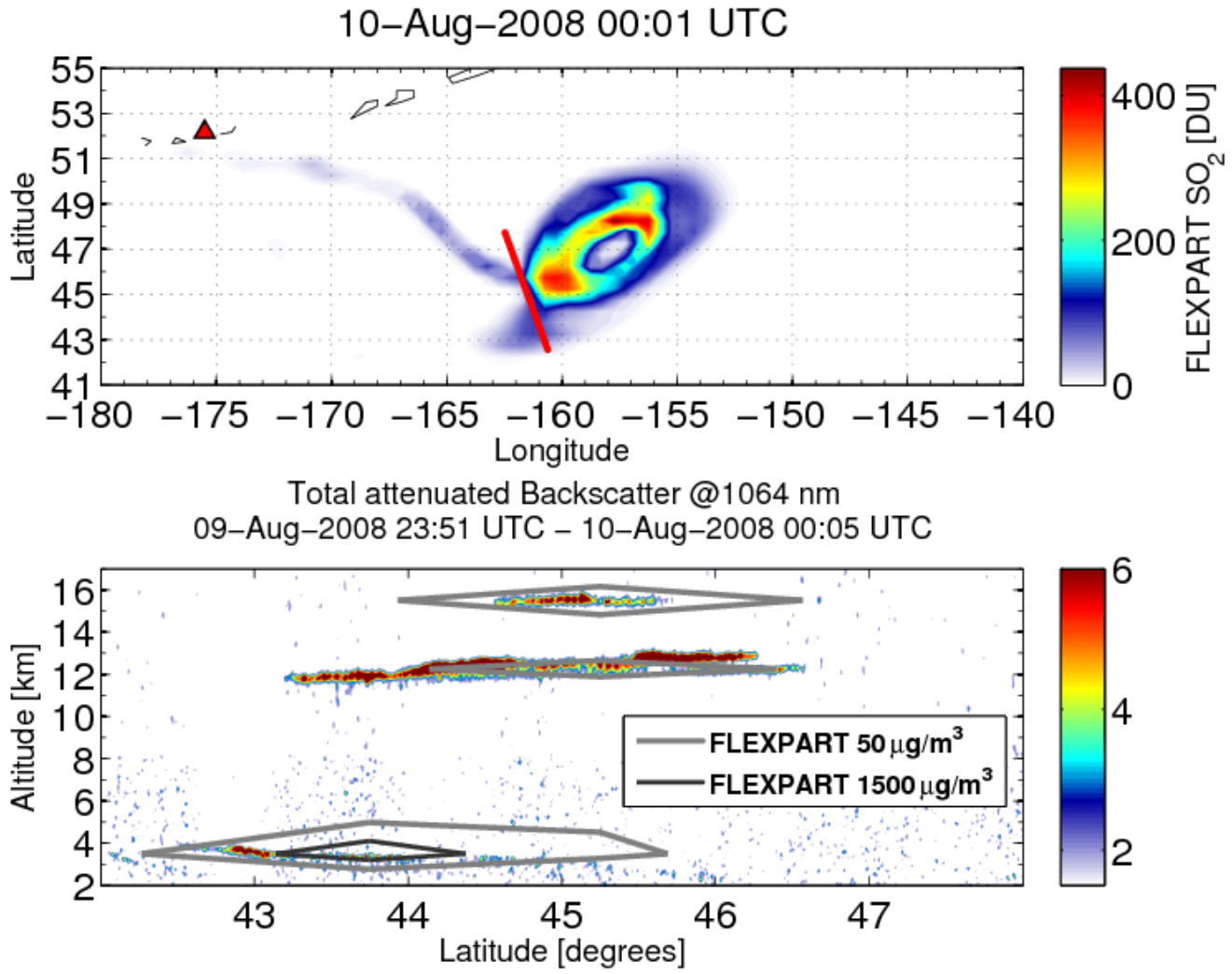


975

976 **Figure 9:** Comparison of CALIPSO attenuated backscatter at 1064 nm with $SO_2$ concentrations
977 simulated by FLEXPART on 9 August. The upper panel shows total columns of $SO_2$ simulated
978 by FLEXPART. The red line indicates the location of the CALIPSO nadir track. In the lower
979 panel, CALIPSO data are shown by the color shadings (in $10^{-3}$ /m sr) and the FLEXPART results
980 are plotted as isolines for 50 $\mu g$ $m^{-3}$ (thick grey line) and 1500 $\mu g$ $m^{-3}$ (thick black line).

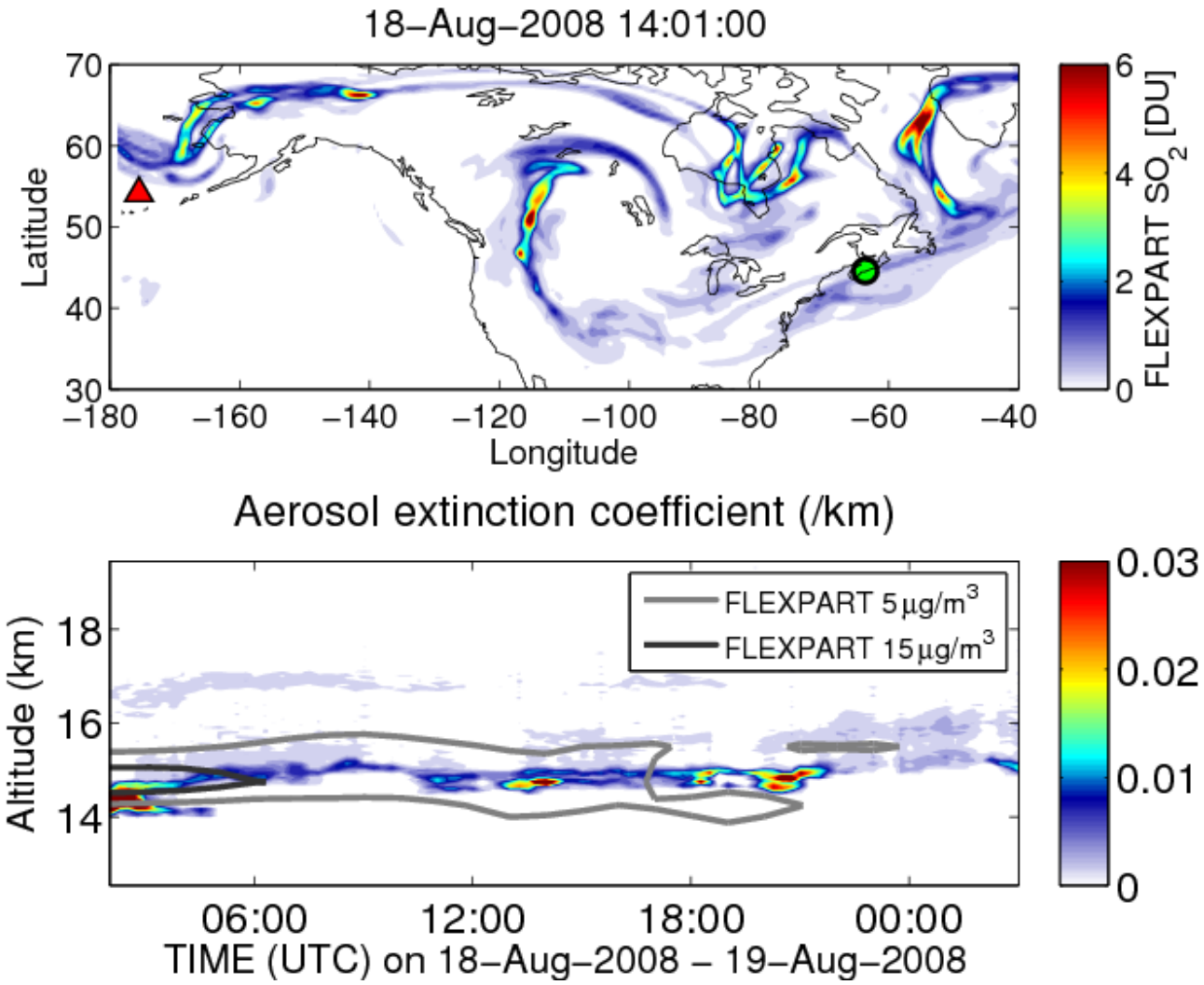


981

982 **Figure 10:** Comparison of aerosol extinction coefficients measured at Nova Scotia on 18-19
983 August and $SO_2$ concentrations simulated by FLEXPART. The upper panel shows total columns
984 of $SO_2$ simulated by FLEXPART from 18 August. The lidar at Nova Scotia is marked with a
985 green dot. In the lower panel, the lidar measurements are shown by the color shadings and the
986 FLEXPART results are plotted as isolines for 5 $\mu g$ $m^{-3}$ (thick grey line) and 15 $\mu g$ $m^{-3}$ (thick
987 black line).

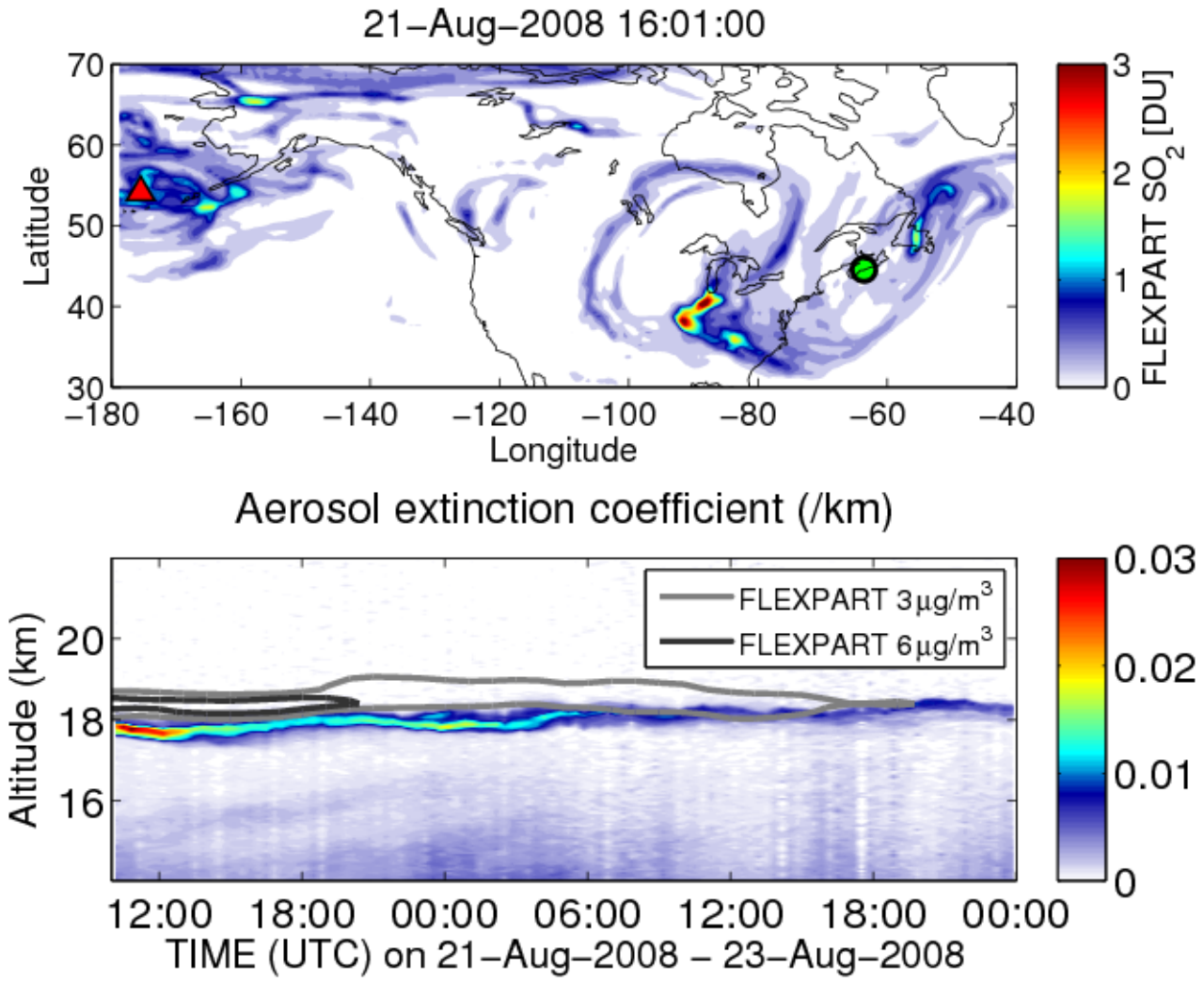


988

989 **Figure 11:** Same as Fig. 10 but for 21-22 August. FLEXPART results are plotted as isolines for

990 3 $\mu g$ $m^{-3}$ (thick grey line) and 6 $\mu g$ $m^{-3}$ (thick black line).

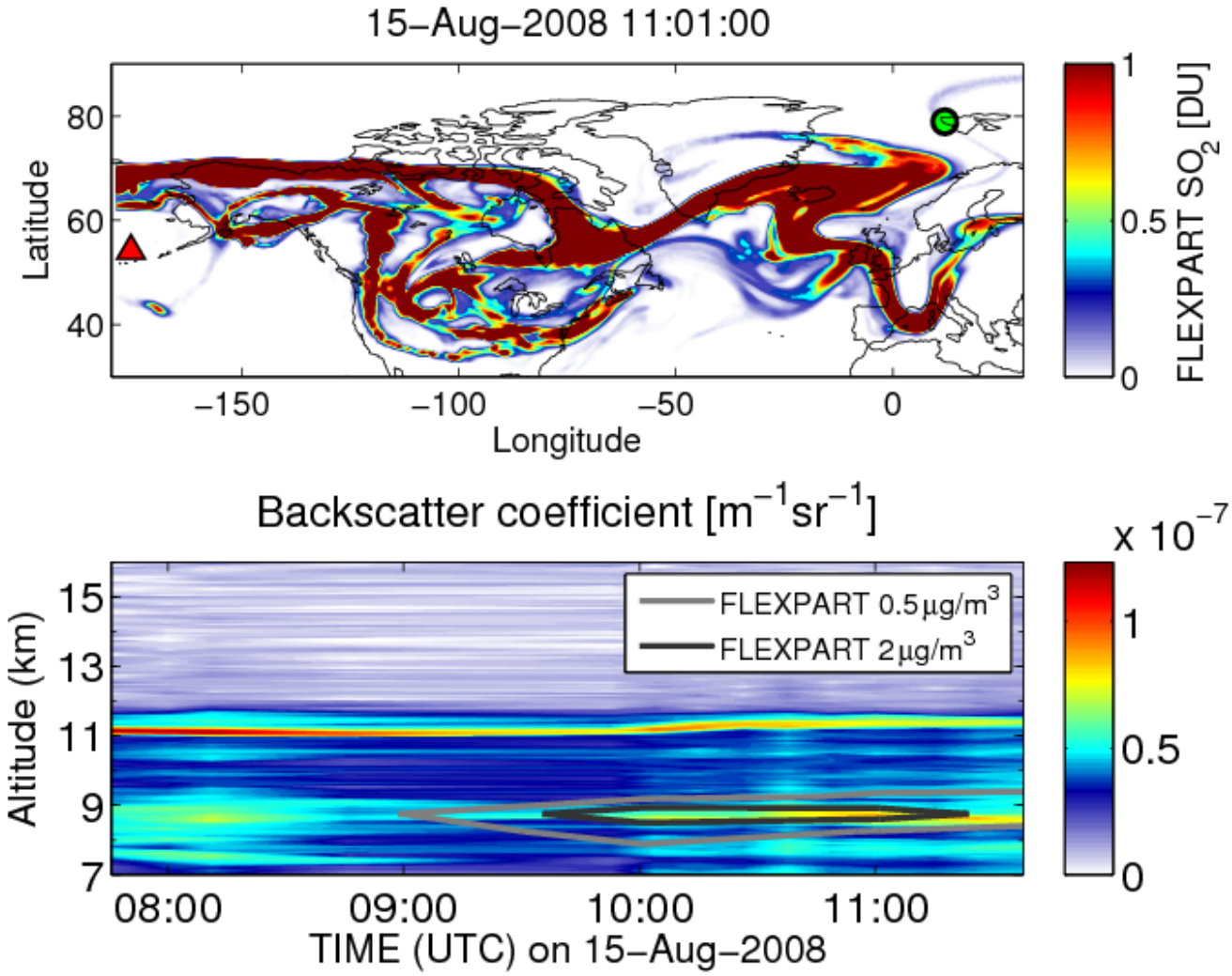


991

992 **Figure 12:** Comparison of aerosol backscatter coefficient measured at Ny Ålesund on 15 August
993 and $SO_2$ concentrations simulated by FLEXPART. The upper panel shows total columns of $SO_2$
994 simulated by FLEXPART from 15 August. The lidar at Ny Ålesund is marked with a green dot.
995 In the lower panel, the lidar measurements are shown by the color shadings and the FLEXPART
996 results are plotted as isolines for 0.5 $\mu g$ $m^{-3}$ (thick grey line) and 2 $\mu g$ $m^{-3}$ (thick black line).

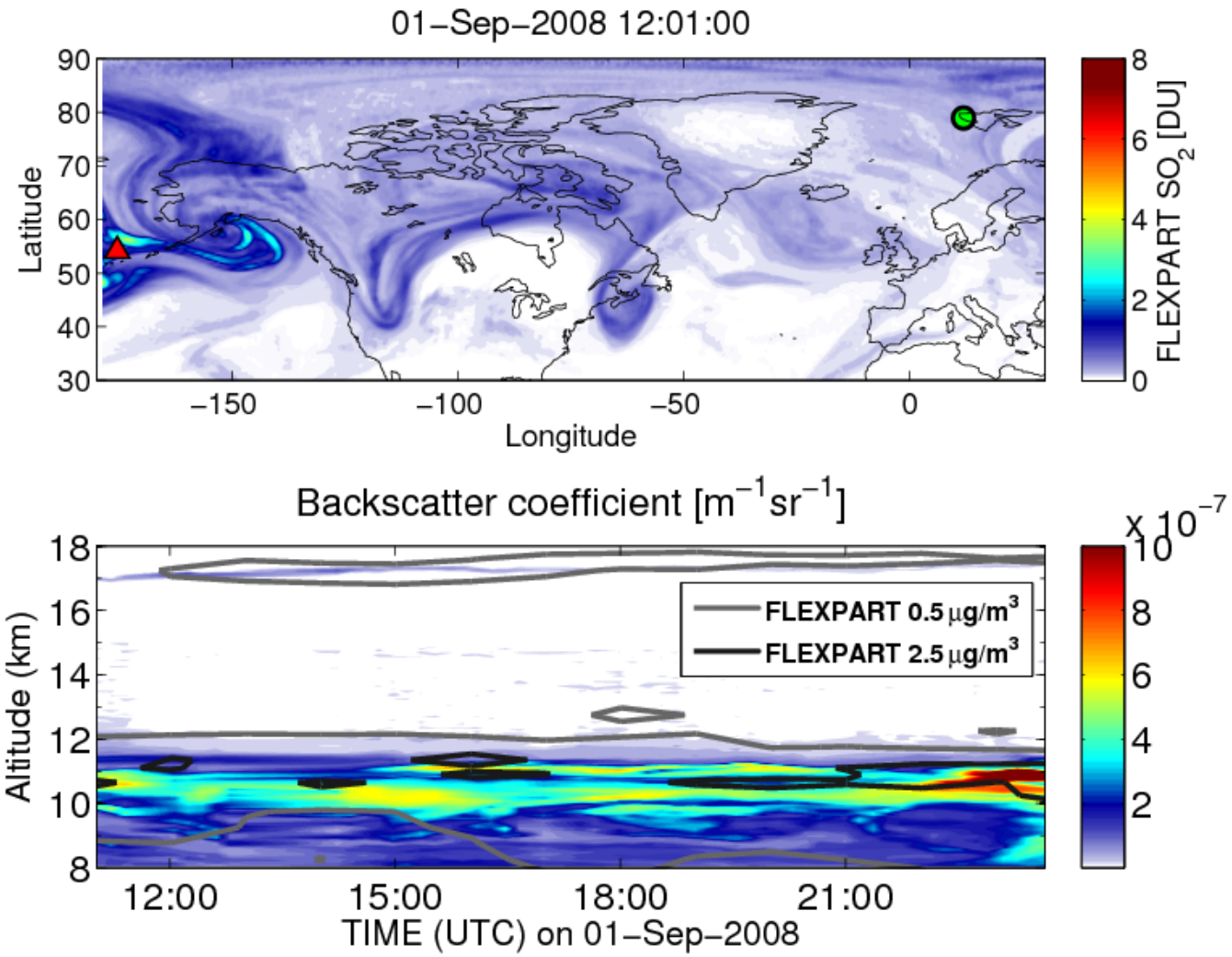


997

998 **Figure 13:** Same as Fig. 11 but for 1 September. The FLEXPART results are plotted as isolines

999 for 0.5 $\mu g$ $m^{-3}$ (thick grey line) and 2 $\mu g$ $m^{-3}$ (thick black line).